AD-A258 996

①

CATHODOLUMINESCENCE SPECTROSCOPY
OF ZINC GERMANIUM PHOSPHIDE
ZnGeP$_2$

THESIS

Michael R. Gregg, Captain, USAF

AFIT/GEP/ENP/92D·04

93-00133

CATHODOLUMINESCENCE SPECTROSCOPY
OF ZINC GERMANIUM PHOSPHIDE
$ZnGeP_2$

THESIS

Presented to the Faculty of the School of Engineering

of the Air Force Institute of Technology

Air University

in Partial Fulfillment of the

Requirements for the Degree of

Master of Science in Engineering Physics

DTIC QUALITY INSPECTED 6

Michael R. Gregg, B.A.

Captain, USAF

December 1992

Accession For

NTIS GRA&I

DTIC TAB

Unannounced

Justification

By

Distribution/

Availability Codes

Dist | Avail and/or Special

A-1

Approved for public release; distribution unlimited

Acknowledgments

The original purpose of this study was to characterize MBE grown antimonides with cathodoluminescence. Unfortunately, that project did not reach fruition and the focus was shifted to the zinc germanium phosphide. This was an exciting challenge because little work has been done on these materials with this technique. It is often possible to lose direction when flying over unfamiliar terrain. I would like to thank my advisors, Maj. P. H. Ostdiek, Dr. R. L. Hengehold, and Dr. Y. K. Yeo for their guidance and encouragement when I needed navigational help.

I would especially like to thank Maj. Ostdiek for his mentorship, and editorial help. I am also indebted to him for repairing the electron gun. I thank Mr. Greg Smith for his technical assistance in keeping the CL system operational and for his many suggestions that helped me get optimum performance from the system. The samples for this study were provided by Dr. M. C. Ohmer of the Materials Directorate of Wright Laboratory. Dr. Ohmer also provided a wealth of information on $ZnGeP_2$ and was very helpful in the analysis of data.

Table of Contents

List of Figures

Abstract

Zinc Germanium Phosphide ($ZnGeP_2$) is a nonlinear semiconductor suitable for use as a laser tuning element over the 2 to 6 μm wavelength range. Although this crystal has been studied in the past, its luminescent properties are not yet well understood. In this present study, $ZnGeP_2$ has been examined using cathodoluminescence spectroscopy (CL). Specifically, the spectral dependence on electron beam energy, beam current, and temperature was obtained. The resulting cathodoluminescence was found to be polarized with peak structure a function of the polarization. This peak structure observed by cathodoluminescence is difficult to detect by photoluminescence (PL). It is believed that the peaks are a direct result of transitions between the conduction band and a spin orbit split acceptor level named Acceptor Level One (AL1). It is also believed that the excitation mechanism is in part responsible for the different structures observed.

CATHODOLUMINESCENCE SPECTROSCOPY OF

ZINC GERMANIUM PHOSPHIDE

I. Thesis Project Framework

1.1 Introduction

This initial chapter builds the framework for the thesis project by providing the motivation for investigating the cathodoluminescence properties of zinc germanium phosphide, and by outlining the project objective and general approach to the research. In addition, the thesis document organization is presented.

1.2 Motivation

1.2.1 Possible Applications

Zinc germanium phosphide ($ZnGeP_2$) is a nonlinear semiconductor crystal that possesses nonlinear optical properties which allow the fabrication of wavelength agile laser systems that emit in the infrared spectral region. These lasers, which are continuously tunable from 2 to 6 microns in an optical parametric oscillator mode, can be used for optical communications when coupled with fluoride glass fibers. The advantage of these systems is that in the 2-4 μm spectral region, signal loss is two to three orders of magnitude lower than in conventional silica fiber systems. (9:607)

What is more important, however, is that lasers operating in the 2 to 6 μm range can exploit atmospheric transmission windows. Additionally, these lasers are eye-

safe and can be used in laser target designator or optical countermeasure systems to defeat infrared imaging systems. To overcome obscurants of haze, smoke, and heavy vegetation, these lasers could also serve as sources in spectral laser radar, or in remote atmospheric sensing. (24:7-9, 25:1)

1.2.2 Roadblocks To Success

Researchers have been aware of the special optical properties of $ZnGeP_2$ that allow fabrication of such laser devices for many years. These properties have not been previously exploited because bulk crystal growth of useful quality and meaningful size was too difficult. In addition, as-grown $ZnGeP_2$ exhibits anomalous absorption at short wavelengths ($< 3\mu m$), which prohibits effective laser wavelength tuning. However, efforts to reduce this absorption by annealing and electron bombardment have proven successful. (24:2) Furthermore, crystal growers have recently applied better bulk growth techniques developed for III-V semiconductors such as gallium arsenide and indium phosphide to $ZnGeP_2$ growth, resulting in higher quality material. (16, 28) Although the bulk crystal growth technology has matured, the lack of a detailed understanding of the material's energy band structure and luminescence properties remains a roadblock to successful system designs.

1.3 Research Objective

The objective of this research is to characterize the luminescent properties of $ZnGeP_2$ and thereby gain a greater understanding of the energy band structure. A secondary goal is to assess the quality of the current $ZnGeP_2$ crystals.

Luminescence is the radiative decay of an excited electron in a semiconductor crystal, and by analyzing the energies of emitted photons, one collects clues to the band structure and impurity energy levels of the crystal. If the material is of low quality, then radiative transitions associated with impurities and crystal lattice defects dominate the spectral response. As a result, spectral data can be used to measure progress in bulk growth and post-growth processing techniques. Knowledge of crystal properties is essential to device design and ultimately to device performance.

Researchers have performed relatively few luminescence studies on $ZnGeP_2$; however, most of those studies that have been done have been centered on photoluminescence (PL) spectroscopy in which the crystal is stimulated by photon absorption. (1:453-457) Cathodoluminescence (CL) spectroscopy is a similar technique in which stimulation occurs when energetic (keV) electrons lose energy to the crystal through collision processes. (33) CL can provide an assessment of impurity levels, dopant concentration, defect levels, carrier lifetimes and charge carrier capture cross

3

sections of impurities. (33:121-159) In addition, crystal
homogeneity can be studied in a non-destructive manner. To
date, only Voevodin et al. are known to have published any
CL data on $ZnGeP_2$. (32)

1.4 General Approach

To accomplish the objective, CL data was taken on three
$ZnGeP_2$ crystals. The general approach was to systematically
change one of the experimental variables while the others
remained constant and determine the effect by analysis of
spectral output. Basic variables available in a
luminescence study are excitation source, samples, and
signal collection and manipulation. In obtaining spectral
output as a function of these variables, electron beam
energy varied from 0.5 to 4 keV, electron beam current from
50 to 200μA, sample temperature from 6.25 to 200 Kelvin, and
the transmission axis of a linear polarizer, through which
the luminescence passed, varied over 180 degrees. The
change in spectra for the different conditions provides the
basis for the analysis.

1.5 Thesis Organization

To help the reader quickly reach the information of
interest, an outline of the written thesis is presented.
The framework of the research project is covered in broad
strokes in Chapter I. Basic solid state concepts and the
theory of luminescence are presented in Chapter II,

including a detailed development of cathodoluminescence. Chapter III discusses the crystal and optical properties of $ZnGeP_2$ and briefly explains its use in an optical parametric oscillator, and Chapter IV contains a description of the apparatus and experimental procedure. The spectral data is presented and analyzed in Chapter V. Conclusions based on the data and recommendations for future investigations follow in Chapter VI. Appendix A is a procedural guide to using the experimental equipment, and Appendix B describes spectrometer calibration procedures. The last section, Appendix C, explains the calculations of the Bethe and Gruen range for electron penetration into the crystal.

1.6 Conclusion

The purpose of the introductory chapter was to set the stage for the actual project. Hopefully, the purpose for performing the study, the goal of the study, and the general approach used to reach the goal are understood. A synopsis of the thesis presentation should aid the reader in locating pertinent information. The next chapter will develop the theory needed to understand the later presentation and analysis of the data.

II. Theory and Background

2.1 Introduction

This chapter presents basic theory to help the reader follow the discussion of the data in Chapters V and VI. The topics include band theory of semiconductors, luminescence in general and cathodoluminescence in particular.

2.2 Basic Concepts of Solid State Physics

2.2.1 Band Theory

Energy band theory is relevant to the study of solids distinguished by their high degree of structural order. Crystalline solids are characterized by long range periodicity of their atomic structure, while polycrystalline solids contain many crystalline regions with different orientations. In contrast, amorphous solids have little, if any, structural order. Crystalline solids are further classified according their electronic energy band structure. A model of the band structure, consisting of forbidden and allowed energy bands, is based on quantum theory.

In quantum theory, an electron is described by a wave function Ψ which satisfies Schrodinger's wave equation:

$$H \, \Psi = E \, \Psi, \tag{1}$$

where H is the Hamiltonian operator

$$H = \left(-\hbar^2 / 2m \right) \nabla^2 + V(r),\tag{2}$$

E is the electron energy, $\hbar$ is Plank's constant divided by 2π, m is the mass of an electron and V(r) is the potential energy function. In the case of an isolated atom, solutions satisfying Schrodinger's equation can be found only for discrete energy eigenvalues. Alternatively, in a crystal composed of many atoms, solutions are found in the form of a continuous energy band structure. The solutions typically begin with Bloch's theorem:

$$\psi_k(r) = e^{ik \cdot r} u_k(r),\tag{3}$$

where k is the propagation vector and $u_k(r)$ is a periodic function with the period of the crystal. The wave functions are well behaved and satisfy proper boundary conditions only if k is real. Energy states associated with imaginary k values are thus forbidden.

When the number of atoms in a crystal becomes very large, the energy levels crowd together. Even though they are still discrete, they can be collectively approximated as quasi-continuous. As a result, alternate bands of allowed and forbidden energy states are formed as shown in Figure 1. (22:213-217) A forbidden energy gap separates the highest filled band, called the valence band, from the next highest band of energy levels, called the conduction band.
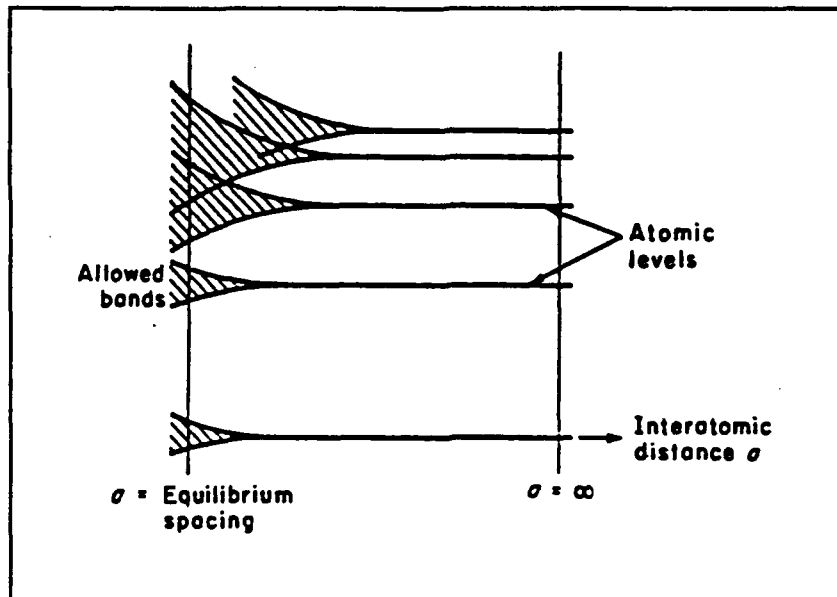
Figure 1. Energy levels in a semiconductor. (22:235)
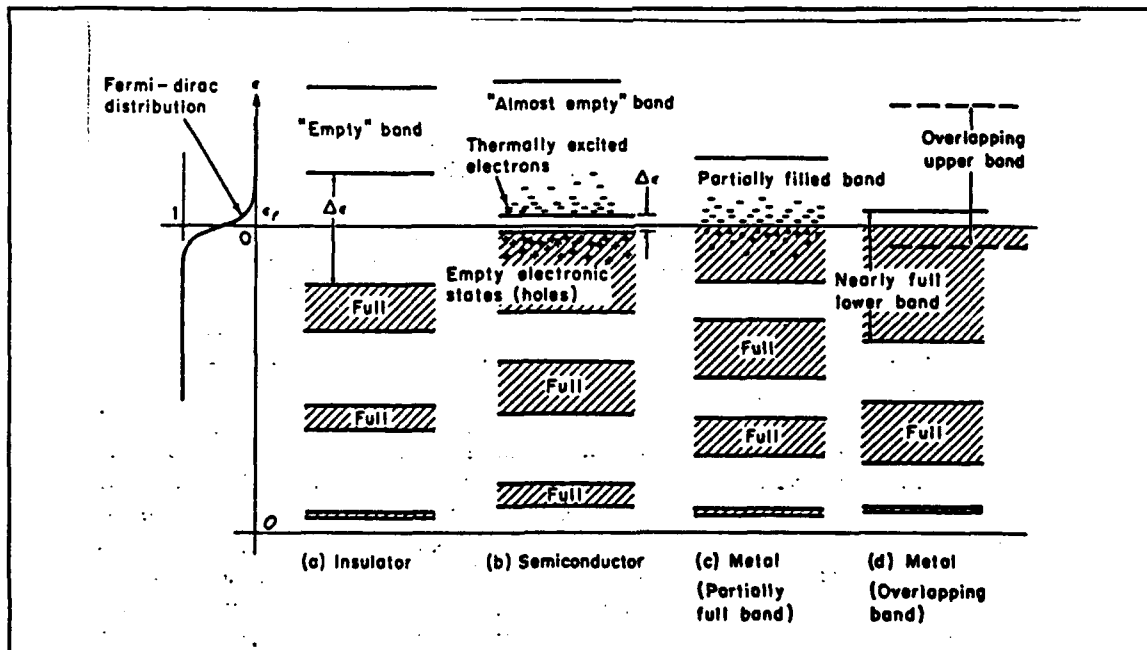
Figure 2. Energy band diagrams for (a) insulator, (b) semiconductor, (c) metallic conductor (partially filled band) and (d) metallic conductor (overlapping bands). (22:246)

8

2.2.2 Insulators, Conductors, and Semiconductors

On the basis of band theory, crystals can be classified as insulators, conductors, or semiconductors. Examples of each are shown in Figure 2. Because the electrons of an insulator exactly fill a number of energy bands, its electrons can not participate in electrical conduction. Since its bandgap energy is so large, electrons can not be thermally excited from valence band to conduction band at realizable temperatures, and therefore, conduction is not possible in an insulator. The conduction band of a conductor is either partially filled or overlaps the valence band. In either case, electrons can readily move to higher energy levels, and current conduction occurs. While a semiconductor may have filled bands, its band gap energy is small compared to that of an insulator so that electrons can be thermally excited to allow conduction. $ZnGeP_2$ is a semiconductor with a bandgap energy of approximately 2.1 eV. (2:330) As temperature rises, electrons in the highest energy states in the valence band can gain enough thermal energy to elevate them into the lowest states in the conduction band. The electron deficiency left in the valence band, called a "hole," behaves like a positive charge, analogous to the negatively charged electron in the conduction band, but with a different effective mass. (22:217-219) Both electrons and holes participate in conduction and are important in luminescence processes.

2.3 Luminescence

2.3.1 Introduction

Electron-hole pair generation in semiconductors plays a vital role in luminescence phenomena. The luminescence process starts when an electron absorbs energy by thermal excitation or from an extrinsic source. It then jumps to an energy level in the conduction band and leaves behind a hole. In some cases the recombination of electron-hole pairs is nonradiative and may occur through multiple phonon emission, the Auger effect (further explained in section 2.4.2), or by recombination due to surface states and defects. The electron may also return to its original state by a radiative transition. A photon is emitted when the electron recombines with a hole left behind in the valence band. Figure 3 illustrates this process.
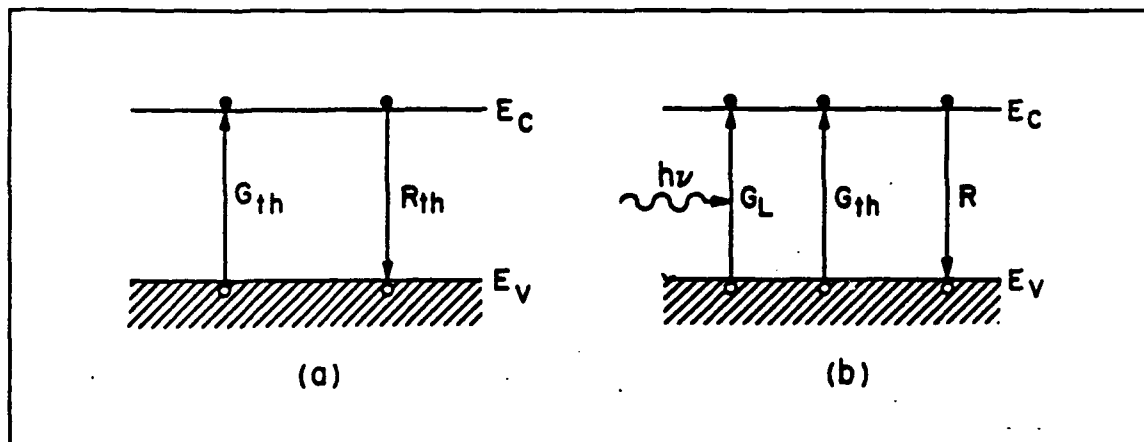
Figure 3. Direct generation and recombination of an electron-hole pair (a) at thermal equilibrium, and (b) under illumination. G_{th} is thermal generation, G_l is photon induced generation, and R is recombination. (31:45)

Such transitions must conserve energy and momentum.

When the minimum in the conduction band and the maximum in the valence band occur at the same value for the wave vector **k**, the transition does not require phonons to conserve momentum and is therefore a direct-gap semiconductor. $ZnGeP_2$ is a direct-gap semiconductor (see section 3.2.2). (7:165) The energy of the photon emitted is the energy lost by the electron.

When the maxima and minima do not coincide, the emission of a phonon is required to conserve momentum. Such material is an indirect-gap semiconductor, and the energy of the photon emitted is the energy lost by the electron minus the energy of the phonon. Figure 4 shows direct and indirect transitions.
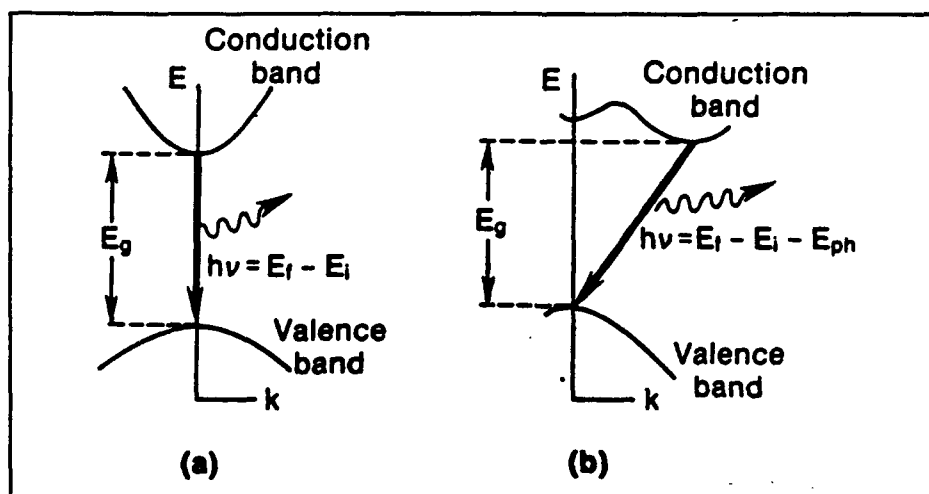
Figure 4. The energy transitions in (a) direct- and (b) indirect-gap semiconductors between initial states E_i and final states E_f. For indirect transitions the participation of a phonon (E_{ph}) is required. (33:23)

2.3.2 Effects of Impurities and Defects

Some luminescent transitions, direct or indirect, involve discrete energy states that exist in the forbidden gap. These states are formed when impurities or crystal defects interrupt the periodicity of the lattice and alter the potential between nearest neighbor atoms. Solutions to the wave equation are then found to exist within the previously forbidden bandgap.

Impurities, whether intentionally added or not, introduce states in the forbidden gap known as donor and acceptor states. Donor states are formed below the conduction band when an impurity has a higher valence than the host crystal and contributes electrons to the conduction band. Acceptor states are formed above the valence band when an impurity has a valence lower than the host crystal and contributes holes to the valence band (or more accurately, accepts electrons from the valence band). In some cases, impurities create states in the middle of the band gap. These states behave symmetrically as sites for either generation or recombination of free carriers. For simplicity they are usually referred to as recombination centers. Crystal defects also introduce states into the forbidden gap. Such defects are usually characterized as point defects or dislocations as shown in Figures 5 and 6.
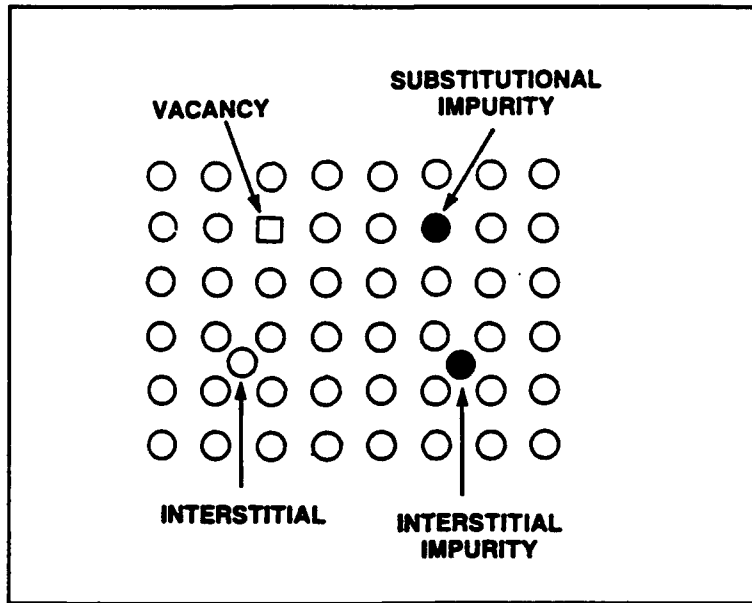
Figure 5. Intrinsic and impurity point defects. (33:16)
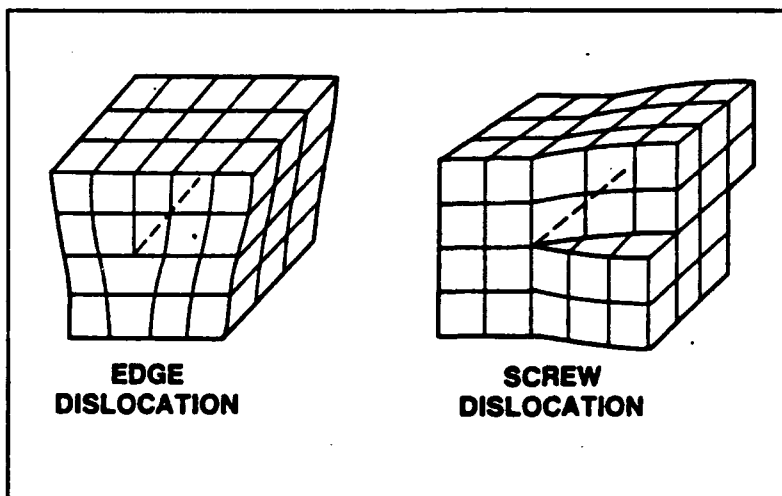
Figure 6. Edge and screw dislocations. (33:17)

13

The effects of point defects including vacancies and interstitials are generally localized. A vacancy is a missing atom in the crystal lattice, while interstitials are extra atoms wedged into the lattice. Since the crystal is deprived of one electron per broken bond, vacancies introduce acceptor states. On the other hand, interstitials introduce donor states because more electrons are available for conduction. Interstitials, vacancies, and impurities may combine to form complexes that may be either a donor or an acceptor.

Edge dislocations and screw dislocations generally extend over many unit cells and may induce significant strain into the crystal. Elastic strain fields may produce shallow levels while dangling bonds may produce deep levels. These effects will alter the intrinsic luminescence properties of the crystal. (33:15-19)

2.3.3 Basic Transitions

The luminescence properties of a semiconductor crystal depend on the energy band structure. Band structure is introduced as a result of atomic periodicity, and its development is based on quantum mechanics. Imperfections in the lattice of atoms cause formation of discrete energy states within the forbidden bandgap. Luminescence occurs when electrons and holes in the allowed energy states recombine to emit photons. Figure 7 illustrates the most common transitions by which luminescence occurs.
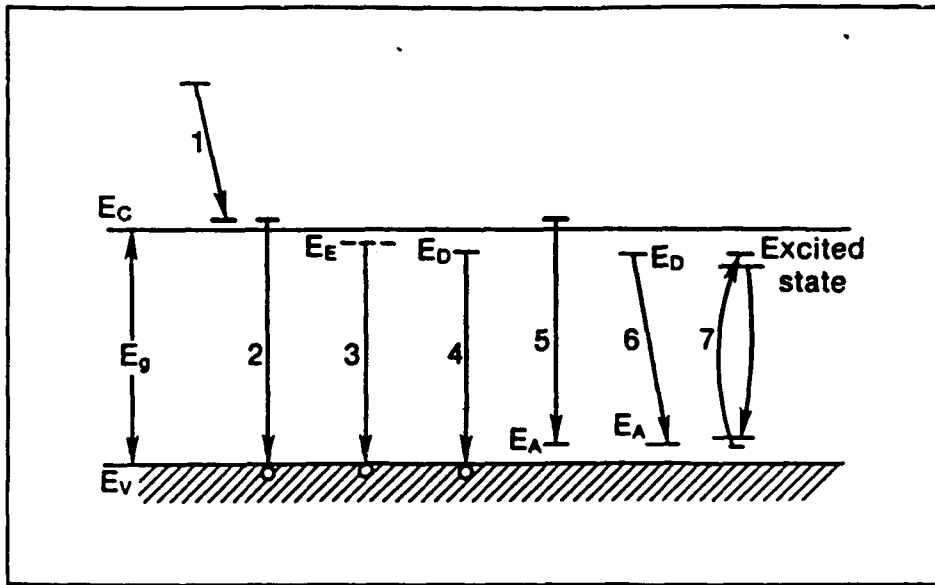
Figure 7. Schematic diagram of radiative transitions between the conduction band (E_C), the valence band (E_V) and exciton (E_e), donor (E_d) and acceptor (E_a) levels in a semiconductor. (33:25)

Process 1 is an intraband transition. The electron loses energy by transferring heat to the crystal through collision processes. This decay usually results in phonon emission.

Process 2 is the fundamental edge emission in which the energy of the photon emitted is greater than or equal to the band gap energy.

$$h\upsilon = E_g \qquad\qquad (4)$$

Band-to-band emission is generally not strong because the photons emitted are readily re-absorbed by the crystal.

Process 3 is an exitonic transition. An exciton is an electron-hole pair linked by coulomb attraction. A free electron and free hole may combine to form a free exciton that can travel through the crystal, and therefore, its energy states are not spatially localized. The electron orbits the hole as in the case of a hydrogen atom, and its energy levels are expressed in a similar manner:

$$E_{ex} = \frac{-m_r^* q^4}{2h^2\varepsilon^2} \frac{1}{n^2}, \tag{5}$$

where m_r^* is the reduced mass expressed as

$$\frac{1}{m_r^*} = \frac{1}{m_e^*} + \frac{1}{m_h^*}, \tag{6}$$

q is the charge of an electron, h is Plank's constant, ε is the dielectric constant, and n is an integer ≥ 1 to indicate various exciton states. In an impurity atom, the effective mass of the nucleus is large, and the reduced mass is equal to that of the electron. In an exciton the reduced mass is lower than the effective mass of the electron because m_e^* and m_h^* are nearly the same order of magnitude. Hence the exciton binding energies are lower than those of donors or acceptors. (27:13) Figure 8 shows the usual convention for placing exciton states into the energy diagram.
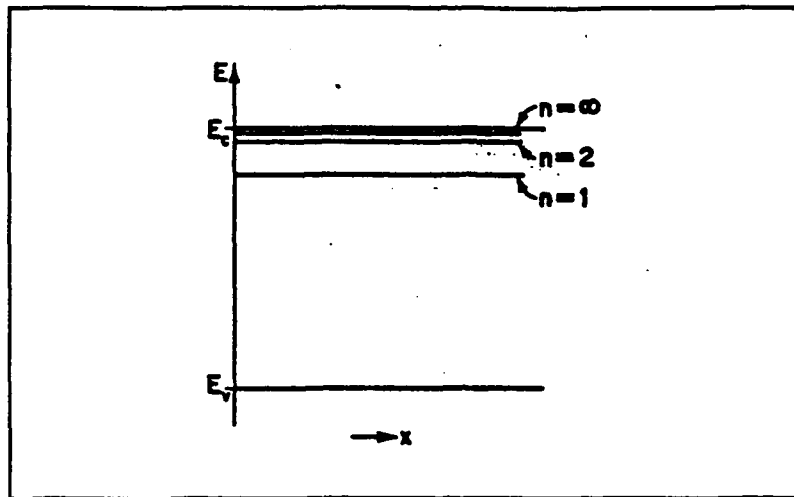
Figure 8. Energy level diagram for the exciton and its excited states, exciton energy being referred to the edge of the conduction band. (27:13)

The photon energy for free exciton recombination is expressed in Equation 7.

$$h\upsilon = E_g - E_{ex} \qquad (7)$$

A free hole can combine with a neutral donor to form an exitonic ion in which the electron associated with the donor orbits the donor as does the associated hole. This electron-hole complex is called a bound exciton since it does not travel through the crystal but is bound to the impurity. The combination of a free electron and the hole on a neutral acceptor will similarly form a bound exciton. Through experiment and by theoretical estimate, the binding energy of a bound exciton is approximately one-tenth the binding energy of the impurity. (13:361, 17:725) The energy

of a bound exciton transition is expressed in the following equation.

$$h\upsilon = E_g - E_{ex} - E_b \qquad (8)$$

Excitonic transitions are very narrow, their FWHM is typically on the order of a few meV's, and their intensities are small. In addition, they are not generally observed at temperatures much above liquid helium temperatures (4 K) because the excitons gain enough energy to dissociate.

Processes 4, 5, 6 represent transitions that begin and/or end with impurity states. Shallow transitions, those that neutralize ionized donors or acceptors, are generally difficult to detect and the photon energies are in the far infrared. A transition of an electron from the conduction band to an acceptor level, or the transition from a donor to the valence band, is a free-to-bound transition. If the transition is direct:

$$h\upsilon = E_g - E_i, \qquad (9)$$

where E_i is the ionization energy of the donor or acceptor level. If the transition is indirect and requires phonon interaction:

$$h\upsilon = E_g - E_i - E_p \qquad (10)$$

where E_p is the energy of the phonon. When the impurity concentration is large enough, impurity levels will merge and overlap the nearest intrinsic band thus creating a difficulty in determining the exact origin of the transition.

When both donors and acceptors are present, coulomb interaction modifies the binding energies and thus affects the photon energy as expressed in Equation 11:

$$h\upsilon = E_g - E_a - E_d + \frac{q^2}{\varepsilon r} \tag{11}$$

where E_a is the acceptor ionization energy, E_d is the donor ionization energy and r is the distance separating the pair. (27:17-18)

Process 7 is the transition of an impurity with an incomplete inner shell, such as a rare earth ion.

Phonon replicas may accompany any of the above transitions producing a sharp emission. Phonon replicas are a series of emission peaks, separated by a phonon energy $\hbar\omega$, created when a recombination process emits one or more phonons along with a photon. As a result:

$$h\upsilon = E_g - E_r - n\hbar\omega , \tag{12}$$

where E_g is the bandgap energy, E_r is the energy depth of the recombination level, $n\omega$ is the phonon energy, and n is

≥ 1. The probability of phonon interaction to produce multiple replicas decreases with increasing number of phonons involved in the emission process. Therefore the line intensity (photon emission rate) of the (n+1)st phonon line decreases as in the following equation:

$$I_n = I_0 \frac{\overline{N}^n}{n!}, \tag{13}$$

where I_n is the intensity of the first line corresponding to photon emission with no phonon participation, and N is the average number of photons emitted in a radiative recombination. (33:43) The intensity of successive phonon replicas should diminish dramatically.

2.4 Cathodoluminescence

2.4.1 Introduction

Many energy sources can be used to generate electron-hole pairs and cause radiative transitions to occur as outlined in the last section. Cathodoluminescence (CL) is the emission of light produced when a material is stimulated by electron bombardment. It is used widely in cathode-ray tube instruments such as televisions or oscilloscopes where the electron beam strikes a phosphorescent screen to produce an image. CL can also be used to perform microscopy or spectroscopy on semiconductors. (18:3-119) Luminescent images of particular regions can be displayed while

20

rastering the electron beam (SEM) in microscopy, and a spectrum from a limited area can be obtained while maintaining a constant beam position in spectroscopy. This study makes use of the spectroscopic CL mode.

CL has a few major advantages over other luminescence techniques. Non-destructive, depth-resolved studies can be performed by changing the electron beam energy. Higher energy beams will penetrate deeper into the sample. (In general, electron beams of energy greater than 100 keV can induce atomic displacement damage. This study uses beam energies between 0.5 and 4 keV.) Depth-resolved studies can be performed to determine crystalline homogeneity or to determine ion-implantation effects as well as to study epitaxial layers in quantum well structures. CL can lead to emission from all luminescence mechanisms in the crystal whereas PL emission may strongly depend on the incident photon energy.

Differences between PL and CL spectra may also arise due to differences in sampling depth. A 40-keV electron beam generates excess carriers to a depth of 3 microns in GaAs while the penetration depth of the photons (1/e distance) is approximately 0.3 microns. (33:72)

2.4.2 Electron Beam Interaction With Solids

Penetrating electrons will lose their energy in a series of elastic and inelastic collisions with lattice ions along the electron trajectories. Back scattered electrons,

21

Auger electrons, secondary electrons, x-rays, phonons, and electron-hole pairs may be produced as a result of the collision process. All of these products are used for micro-characterization purposes.

The elastic scattering process can be analyzed by the Rutherford model. (12:108-114) Elastic scattering leads to back scattered electrons with energies close to that of the incident electrons. They come from within a micron of the surface. When the back-scattered electrons are used for scanning electron microscopy (SEM) purposes, they can provide atomic number contrast. Atoms with a larger atomic number have a larger scattering cross section and thus are more efficient scattering centers. These atoms will appear brighter on a CRT display.

Inelastic scattering can produce many signals useful for micro-characterization. Auger electrons absorb the energy released by recombining electrons and are excited to higher energy states. They are subsequently emitted from the semiconductor or they dissipate the energy through emission of phonons. Since Auger electrons are emitted from the top 10 angstroms of the surface and have energies characteristic of the elements of the material, Auger spectroscopy can aid in surface analysis.

Secondary electrons are generated by electron beam interaction with conduction band electrons. They are emitted with energies less than 50 eV and originate within 50 angstroms of the surface. Secondary electrons are used

for SEM because they can provide topographical contrast with better resolution and depth of field than optical microscopes. (18:39)

X-rays are emitted when an electron makes a transition between sharp, inner core levels. X-rays can be used to determine concentrations of elements within the electron-excited volume.

Phonons will dissipate the electron energy non-radiatively and may affect electron-hole recombination as expressed in section 2.3.3.

Electron-hole pair generation is of primary interest for this study. The pairs are generated when an electron in the valence band absorbs enough energy from the penetrating electron to jump into the conduction band. The subsequent radiative transitions, as outlined in section 2.3.3, produce the desired luminescence spectrum.

2.4.3 Electron Energy Loss and Penetration

Many electron-hole pairs are generated when the electron beam penetrates the crystal. As previously stated, penetration depth depends on the beam energy. The mean rate of energy loss per segment of distance S traveled in the solid is expressed by the Bethe equation

$$\frac{dE}{dS} = -2\pi\, q^4\, N_A\, \frac{\rho Z}{EA}\, \ln\left(\frac{1.166\, E}{J}\right), \qquad (14)$$

where q is the electronic charge, N_A is Avogadro's number, ρ is the density, Z is the atomic number, A is the atomic weight, E is the mean electron energy, and J is the average energy loss per interaction. (33:57)

$$J = \left(9.76\,Z + 58.5\ \ Z^{-0.19} \right) 10^{-3}\ (\,\text{keV}\,) \qquad (15)$$

Making the approximations $\rho = 4.13$ g/cm^3, Z = 23, and A = 199.92 g/mol in ZnGeP$_2$, an electron with 3 keV energy, when it impacts the crystal surface, will lose 9.23×10^{-4} keV per angstrom traveled. (See Appendix C for a more detailed development.) The electron would travel a total "random walk" distance of 0.92 microns before its energy dissipates. Obviously the electron will not travel in a straight line but will approximate the trajectory found through Monte Carlo simulations illustrated in Figure 9.

The Kanaya-Okayama variation of the Gruen range equation estimates the effective penetration depth of the impinging electrons, or distance traveled in the direction parallel to the electron beam. (19:43)

$$R_e = \left(\frac{0.0276\,A}{\rho Z^{0.889}} \right) E^{1.67}\ (\,\mu\text{m}\,) \qquad (16)$$

The penetration range for a 3 keV electron in ZnGeP$_2$ is 0.51 microns. See Appendix C for further discussion of energy dissipation, penetration range and excitation volume.
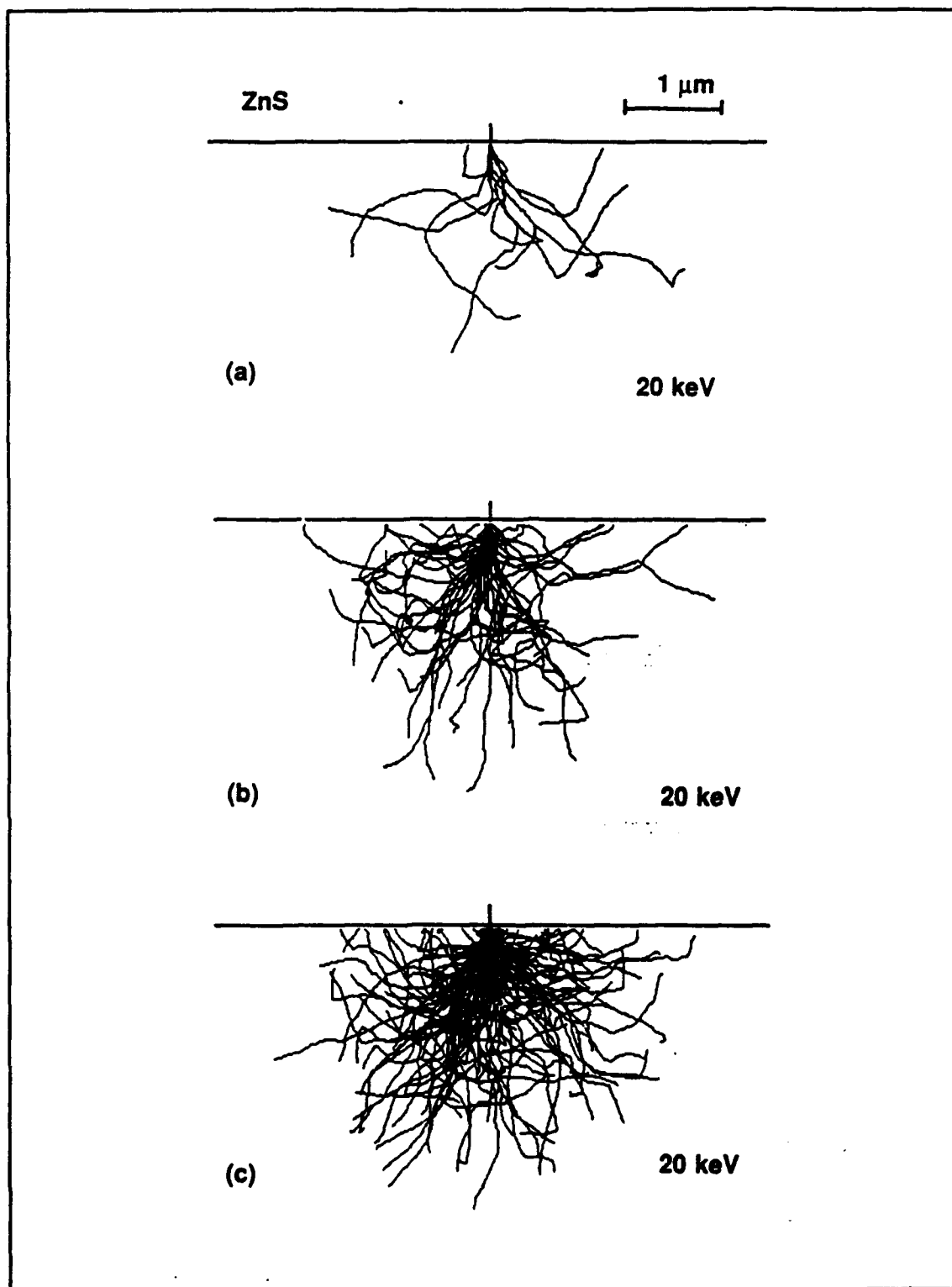
Figure 9. Trajectories of (a) 10, (b) 50, and (c) 100 electrons of 20 keV calculated by the Monte Carlo method for ZnS. (33:63)

When intensity and efficiency are relatively unimportant, low electron energies will allow maximum beam deflection sensitivity or better positioning. (20:427-428) However, a low energy threshold exists where the electrons lack sufficient energy to penetrate the surface layer and overcome the effects of surface recombination or to overcome the repulsive force generated by secondary electrons. Thus a trade-off exists between beam positioning and sufficient signal generation. Proper electron energies can only be determined through the experimental process.

2.5 Conclusion

Luminescence occurs when electrons, having been excited to non-equilibrium energy states, make a radiative transition to a lower energy state. The states available to the electrons are described by quantum theory. Absorption of energy from an impinging beam of electrons is the excitation mechanism for CL. Intensity of the light emitted versus wavelength, or photon energy, is recorded to produce a spectrum used to determine the properties of the crystal.

III. Properties of Zinc Germanium Phosphide

3.1 Introduction

This chapter presents basic properties of zinc germanium phosphide ($ZnGeP_2$) and how these properties are used to make laser devices. Topics included are crystal growth, crystal structure, optical properties, and optical parametric oscillators.

3.2 Crystal Properties

3.2.1 Crystal Growth

The samples used in this study were grown by the Bridgman or Gradient Freeze method. (11:85, 28) The growth process begins by loading the individual constituents, or a polycrystalline ingot, in a long boat. The boat is usually made of quartz and is sometimes coated with a pyrolytic carbon film to protect the walls from the growth constituents during prolonged heating. After the constituents are loaded, the boat is evacuated and then backfilled with an inert ambient gas, usually helium. The boat is placed into a furnace and the system temperature is brought up to the melting point of the crystal. A temperature cycle may include many ramp and soak steps before growth is initiated. After the constituents are thoroughly reacted, the quartz tube is slowly pulled from the furnace, setting up a temperature gradient across the melt constituents as shown in Figure 10. As the tube is

pulled, a single grain is formed at the cooled end (or a
seed crystal is used), and growth propagates from the
liquid-solid interface. Eventually the entire melt is
frozen to form a single crystal boule as in Figure 11.
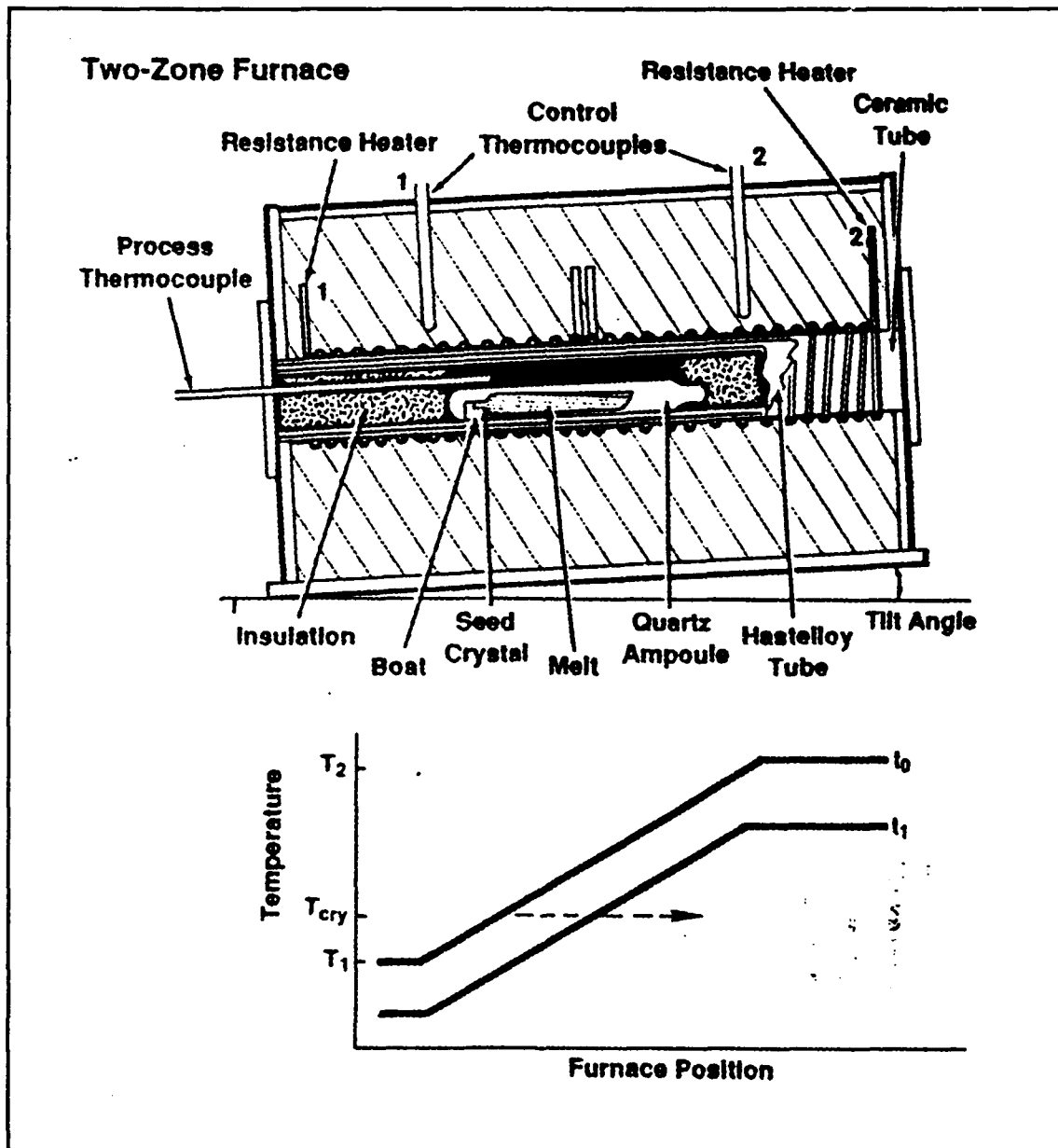
Figure 10. Schematic illustrating crystal growth by
horizontal gradient freeze technique. (28:32)
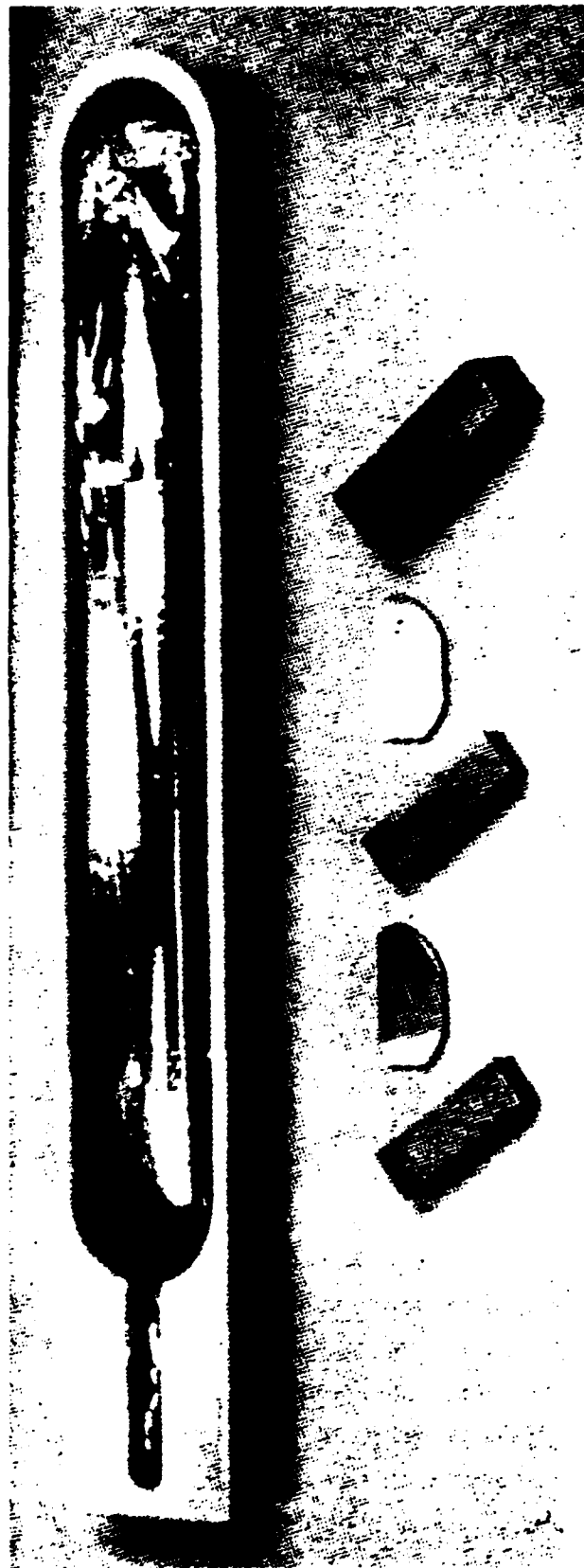
Figure 11. ZnGeP$_2$ single crystal grown by the horizontal
gradient freeze technique. (28:35)

The samples in this study were cut from such a single crystal boule. However, the orientation of the c axis is not known.

All Bridgman crystals grown to date have been p-type and semi-insulating.(25:3) The semi-insulating character has been attributed to a deep acceptor with a concentration on the order of $10^{19}/cm^3$ and an ionization energy near 0.6 eV. (6:379) This acceptor level may result from intrinsic defects such as a germanium vacancy and a zinc antisite. This native acceptor has been designated as Acceptor Level 1 (AL1). (25:3)

3.2.2 Crystal Structure

The as-grown $ZnGeP_2$ crystal is a semiconductor with a chalcopyrite structure. Chalcopyrites are composed of elements from columns II, IV, and V of the periodic table, and they represent an extension of the III-V zinc-blende compounds as shown in Figure 12. Alternate cation sites are occupied by the zinc and germanium along the c axis. The phosphorous atoms are in a tetrahedral arrangement, displaced slightly from their zinc-blende positions. The lattice constant a is 5.465 angstroms, and the lattice constant c is 10.771 angstroms. (7:162) Bonding in $ZnGeP_2$ is predominately covalent which is, in large part, responsible for the large nonlinear optical coefficients in these crystals. (21: 2591-2600)
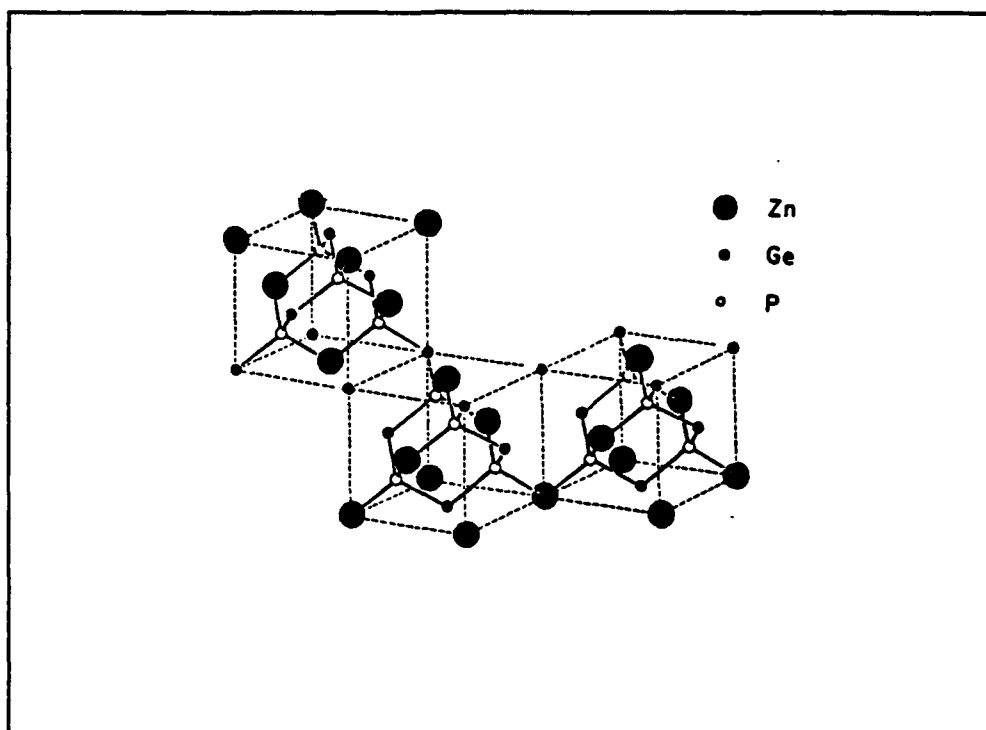
Figure 12.   Crystal Structure of $ZnGeP_2$. (7:161)

ZnGeP$_2$ is a ternary analog to gallium phosphide (GaP).
However, theory suggests that the ZnGeP$_2$ is a direct gap
semiconductor while GaP is an indirect. (30:983)   The
chalcopyrite real-space unit cell can be envisioned as two
zinc-blende unit cells joined and slightly compressed along
the c axis.   Since the lattice constant along the c axis is
effectively doubled, and the Brillouin zone goes as π/c, the
Brillouin zone for the chalcopyrite can be obtained by
folding down the first Brillouin zone of the zinc-blende
crystal.   As a result, the band gap that was indirect in the
ternary, becomes pseudo-direct in the chalcopyrite.   The
band gap energy for ZnGeP$_2$ has not been definitely

established. Many different values are reported in the
literature, but 2.1 eV at 77K seems to be a good approximate
figure. (2:330, 32:148, 10:106, 4:301) Figure 13 shows a
theoretical band structure, and Figure 14 illustrates the
triplet state of the valence band.
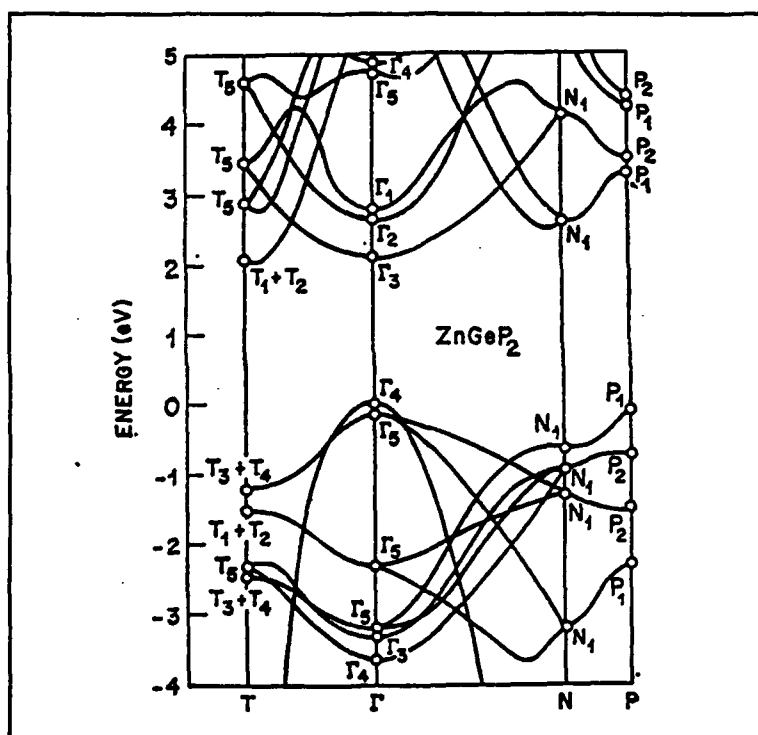
Figure 13. Theoretical energy band structure for ZnGeP$_2$
(30:81)
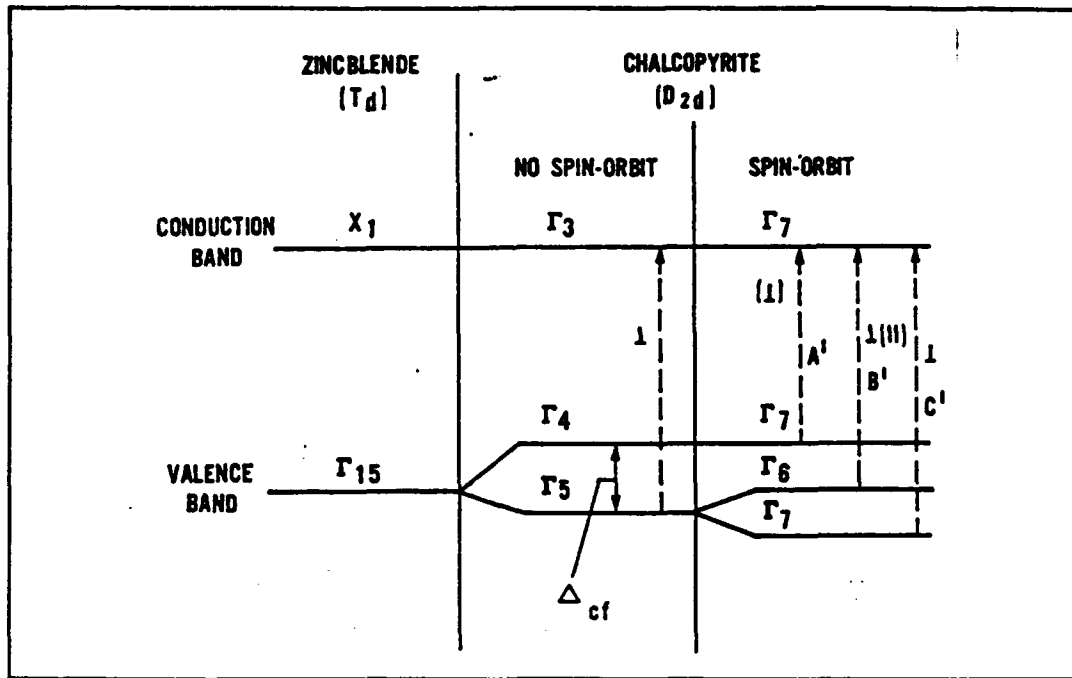
Figure 14. Band structure and selection rules for pseudo-direct transitions in a chalcopyrite crystal.(30:91)

3.3 Optical Properties

The crystalline properties of $ZnGeP_2$ lead to some interesting optical properties. $ZnGeP_2$ is birefringent, displaying two different indices of refraction as a result of dielectric anistropy. The phase velocity of an optical beam propagating in the crystal depends on the direction of the polarization of its **E** vector. A beam polarized normal to the c axis, also known as the optic axis, will propagate at a different speed, v, from a beam polarized parallel to the c axis:

$$v = \frac{c}{n} ,$$

(15)

$$n = \sqrt{K_e K_m} ,$$

(16)

33

where n is the index of refraction, K_e is the relative
permitivity or static dielectric constant, and K_m is the
relative permeability. Any optical beam incident on a
birefringent crystal with components parallel and
perpendicular to the c axis will emerge elliptically
polarized. The exiting beam can then be decomposed into two
orthogonal beams, the ordinary ray (o-ray) and extraordinary
ray (e-ray). The o-ray is the component of the beam
polarized normal to the c axis, and will traverse the
crystal unrefracted. The e-ray is the component of the beam
that has been refracted. It will emerge parallel to
propagation axis and will be polarized orthogonal to
polarization direction of the o-ray. See Figure 15.
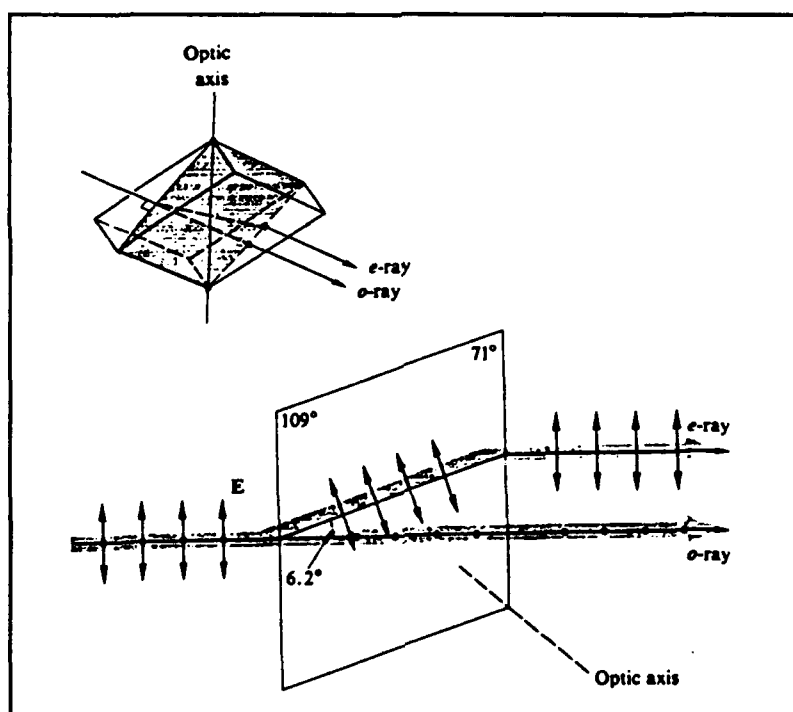
Figure 15. A light beam with two orthogonal field
components traversing a birefringent crystal. (14:286)

34

As a result of the birefringent properties, emitted light from a ZnGeP$_2$ crystal is generally polarized. This study observes and reports on this phenomena.

It has been reported that AL1 is polarization dependent. (24:1) The absorption coefficient for the extraordinary ray is larger than that for the ordinary ray for photon energies greater than the AL1 ionization energy. The as-grown ZnGeP$_2$ crystal has high anomalous absorption near the band edge as shown in Figure 16. Recent efforts to reduce the absorption have centered on annealing processes and bombardment with high energy electrons. (24:1)
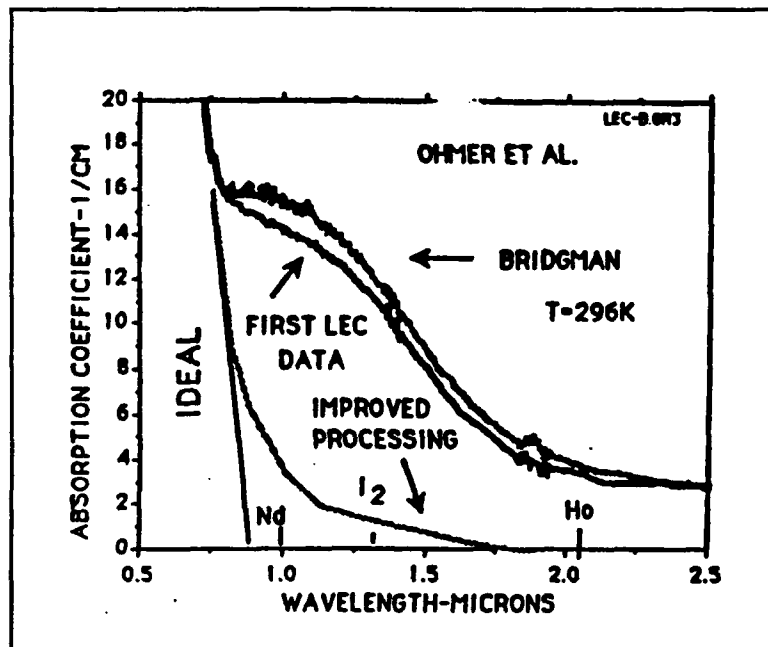
Figure 16. Intrinsic absorption near band gap and effects of improved processing. (24:1)

As previously stated, $ZnGeP_2$ is a nonlinear material. This nonlinearity can be put to good use as seen in the next section.

3.4 Optical Parametric Oscillation

In most crystals, the polarization induced by the propagation of electromagnetic radiation through the media is linearly proportional to the electric field. $ZnGeP_2$ is a nonlinear material in that electromagnetic radiation passing through $ZnGeP_2$ will produce a polarization proportional to the square of the electric field in addition to the linear response. This nonlinear property is used in optical parametric oscillators (OPOs) to tune laser output over a continuous frequency range determined in large part by the absorption properties of the crystal. If a nonlinear crystal is pumped with a beam of frequency ω_3, simultaneous amplification of "signal" and "idler" waves at frequencies ω_1 and ω_2 (where $\omega_3 = \omega_1 + \omega_2$) will occur if the crystal is placed in an optical oscillator that provides resonance for the signal and/or idler waves. Parametric gain will cause a simultaneous oscillation at the signal and idler frequencies. The pumping threshold corresponds to the point at which the parametric gain balances the losses in the cavity. Signal and idler frequencies can be tuned by changing the angle between the c axis and resonator axis (34:294) as shown in Figure 17. Continuous tuning can also be obtained in (OPOs) with fixed values of both pump

frequency and c axis orientation by temperature variation of refractive index to change phase matching conditions. (4:301-304)
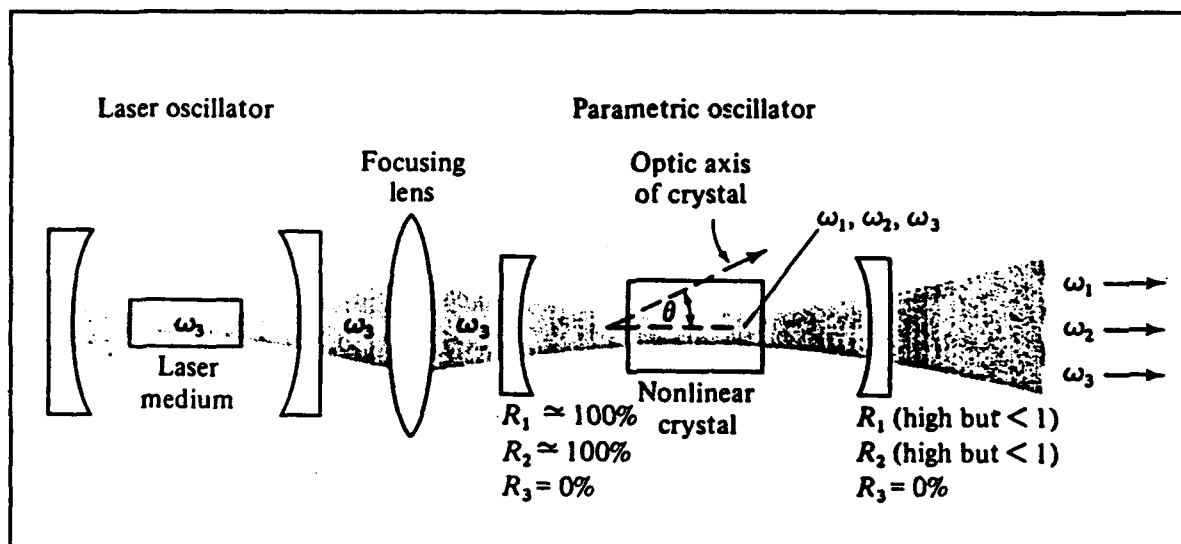
Figure 17. Schematic diagram of an optical parametric oscillator in which the laser output w_3 is used as the pump, giving rise to oscillations at w_1 and w_2 in an optical cavity that contains the nonlinear crystal and resonates at w_1 and w_2. (34:294)

3.5 Conclusion

ZnGeP$_2$ has many interesting nonlinear and polarization dependent properties. These properties can be exploited to make tunable lasers in the infrared, however they have not been fully exploited at this time because high quality crystals have been difficult to grow. New processes have recently emerged to grow large, single grain boules, and post growth processing techniques are being developed to improve the absorption properties to allow frequency tuning in the parametric oscillator mode from 2 to 6 microns. This

CL study will help provide a fuller picture of properties of the crystal and may provide insight into the effects of post-growth processing. The next chapter will explain how the CL data was obtained.

IV. Equipment and Procedures

4.1 Introduction

The equipment and procedures used to obtain the CL data are detailed in this chapter. Individual components and their use in the collective system are described. Experimental procedures, to include data collection, storage and reduction, are discussed.

4.2 Equipment Used

4.2.1 Brief System Overview

A schematic of the entire CL system is presented in Figure 18. Samples were placed at the end of a sample holder, the sample holder was then inserted into the vacuum chamber which was evacuated by a pump system. After reaching a suitable low pressure, the samples were cooled by a liquid helium transfer system and excited by an electron beam from an electron gun mounted in the vacuum chamber. The luminescence resulting from this excitation was collected by a lens system and focused into the spectrometer. A photomultiplier (PMT) picked up the luminescence from the spectrometer, and generated an output current which was converted into a voltage and then fed to a lock-in amplifier. The output of this amplifier was sent to a computer where it was stored for future use.
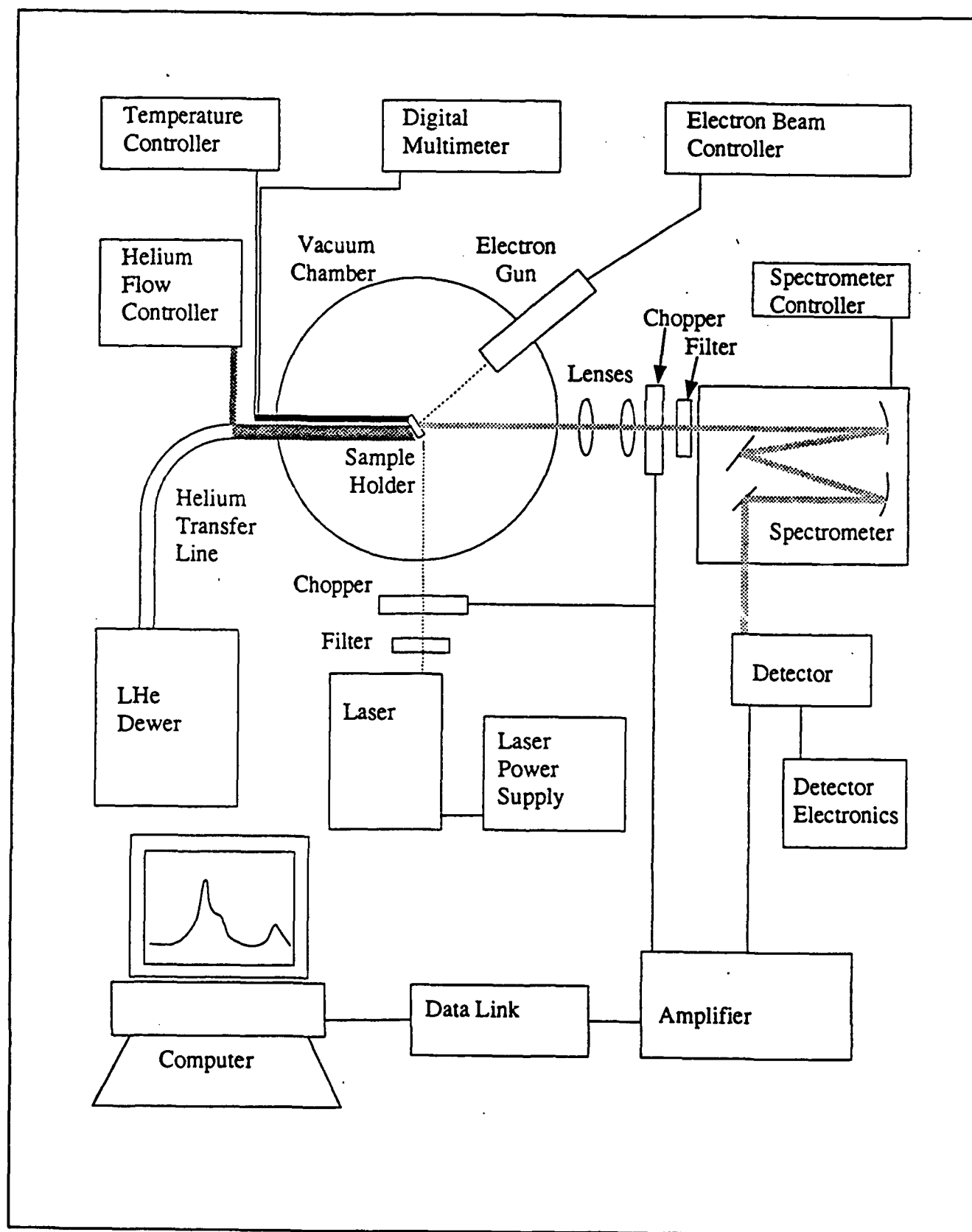
Figure 18. Schematic diagram of the CL system. (8:45)

4.2.2 Sample Holder And Cryogenic System

The samples were mounted on a copper block, which had a front and back mounting surface, one sample to a side. A silicon diode was mounted on one of the faces to provide an accurate temperature reading. In addition, a gold-chromel thermocouple was inserted into the block to serve as another temperature reference but did not agree with the diode and is believed to be inaccurate. The diode and a resistive heater, located just above the block, were controlled by a Lakeshore 330 Autotuning Temperature Controller. Sample temperature could be varied between 6.25K and 200K. Below 15K the temperature could be controlled within 1.0K, and above 15K the temperature could be controlled within 0.5K. The low temperatures were needed because luminescence peaks intensify and narrow with decreasing temperature.

Low sample temperatures were obtained by the use of a an Air Products model LT-3-110 Helitran System which basically consists of a coldfinger and liquid helium transfer line. The coldfinger, at the end of which sits the sample holder, is essentially a long, thin dewar which is inserted into the vacuum chamber. Two viton o-rings seal the coldfinger in the chamber but allow it to rotate for sample alignment. A transfer line, comprised of two capillary tubes, inserts into the coldfinger. The center tube, or cryo-tip, transfers liquid helium to the sample holder. The second tube, or shield, is required to keep the first tube cold and promote a steady flow of liquid helium

to the sample holder. Exhaust gasses from the cryo-tip and shield were routed to flow controllers. Gas flow through the controllers was used to control the liquid helium flow.

4.2.3 Pump System and Vacuum Chamber

After the samples were placed in the vacuum chamber, but before cooling down, the chamber was evacuated below 5×10^{-7} torr. If the electron gun is operated at higher pressures, the filament used to produce the electron beam will rapidly oxidize and burn out.

An Alcatel, direct-drive mechanical pump was used to rough pump the chamber, then an Alcatel Type 5081 turbomolecular pump was turned on. Once the pressure was below 1×10^{-5} torr, a Varian 220 liter/second Noble VacIon pump with model 921-0043 Pump Control Unit was turned on, and the valve between the chamber and turbo-pump was closed. The VacIon, along with a Varian model 916-0017 Titanium Sublimation Filament Cartridge with model 922-0032 Pump Control Unit, could maintain a vacuum of 5×10^{-9} torr. Pressure in the chamber was measured with a Granville-Phillips ionization gauge, or determined from the current drawn by the VacIon pump. Figure 19 illustrates the pump system.

The vacuum chamber itself was cylindrical, 0.3 meters in diameter, 0.67 meters in height. (29: 53) It was divided into an upper and lower half. The lower half contained

42
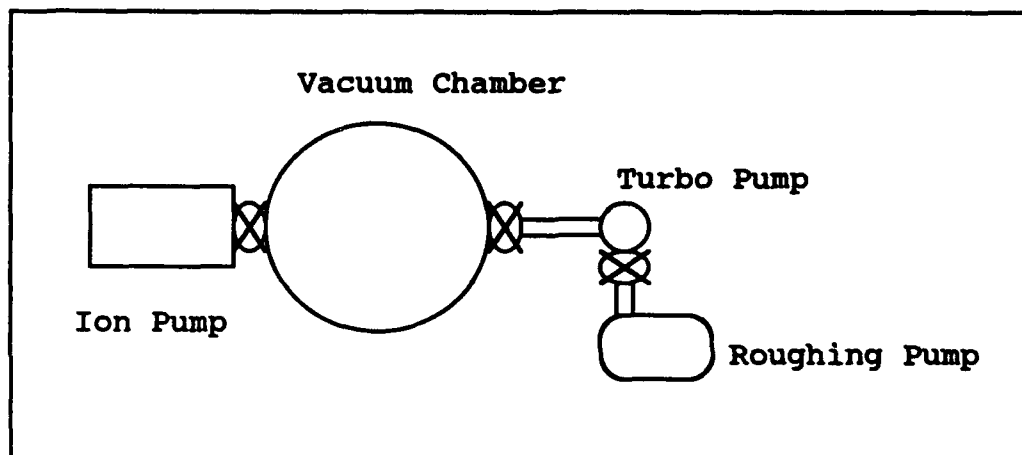
Figure 19. Schematic diagram of pump system.

electrical feedthroughs and pump ports. The upper chamber had four large (8-inch) and four small (2.75 inch) ports. One port contained the electron gun. With the exception of three optical windows, the rest of the ports were blanked off. Two of windows were pyrex. A laser was fired through one, while the other was used as an observation port. A third window was made of sapphire and luminescence from the sample exited the chamber through this port.

4.2.4 Excitation Sources

Both cathodoluminescence and photoluminescence were observed in this study; however, most of the work centered on electron beam excitation. A VG Microtech Leg 32 Electron Gun was the electron source. The gun was mounted 45 degrees from the exit port with the tip of the gun approximately 5 cm from the sample holder. The beam was controlled by a

Model 326A power supply, and was electrostatically focused to a spot size on the order of millimeters.

Although beam energies could be varied from 0.1 to 5 keV in steps of 0.1 keV, 4.5 keV proved to be a practical limit. After extended use above this voltage, the high voltage circuit breaker would trip off. Variation of beam energy yields a variation of electron penetration depth into the crystal. As discussed further in Section 2.4 and Appendix C, a 1 keV beam is expected to penetrate 0.1 microns into the crystal while a 4 keV beam penetrates 0.8 microns.

The beam current could be varied from 2 to 1000 μA with 500 μA proving to be a practical limit since the white light produced by the filament at current levels needed to produce 1000 μA beam currents also created a large background signal in the luminescent spectra. (Beam currents reported are those measured by the circuitry of the Model 326A power supply. These currents were not independently confirmed by a Faraday Cup in the chamber.) Beam current is changed to vary the electron density. (18: 17) More electrons will strike the sample surface with increasing beam current, and thus the intensity of the luminescence will increase.

Luminescence was also excited by photons from a Spectra-Physics, Model 161B-07 Argon Ion Laser. The photons produced at 488 nm with a measured power of 30 mW at the exit port of the laser, entered the chamber through a window mounted at an angle of 90 degrees to the exit port.

4.2.5 Optical System

After the luminescence was generated, by either the electron beam or laser excitation, it exited the chamber through a sapphire window and was collected by a 25 cm focal length, calcium fluoride lens, 2 inches in diameter, placed close to the window. The 25 cm focal length was chosen to coincide with the distance from the sample to the outside of the sapphire window. Since the origin of the luminescence could be approximated to be a point source, the light was approximately collimated after passing through the lens. (14:139) This collimated luminescence was then focused onto the entrance slit of the spectrometer by a 15 cm focal length glass lens, 2.5 inches in diameter, placed approximately 15 cm from the entrance slit. A linear polarizer was placed after the second lens and mounted on a rotating stage so that its transmission axis could be rotated through angles normal to the optical path. The luminescence signal was then chopped by a Stanford Research Model Sr540 Chopper Controller at a typical chopping rate of 100 Hz.

4.2.6 Signal Detection and Processing

After the luminescence was collected by the optics and chopped, it was passed through a Spex 500M Spectrometer employing a 4 square inch, Milton-Roy grating blazed at 1 μm with 1200 grooves/in. The rotation of the grating was controlled by an MSD 2 controller and was most often scanned

45

from 7000 to 11500 angstroms. The MSD 2 allowed a continuous range of scan speeds, but the scan speed used in this study was always 226 angstroms/minute. A 9684, S1 PMT detected the luminescence diffracted from the grating. The PMT was run at 1000 volts by a Keithley 244 High Voltage Supply and cooled by a Products For Research liquid nitrogen transfer system to improve the signal-to noise ratio. The output from the PMT was fed to a Keithley 427 Current Amplifier and then into a Stanford Research Systems SR510 Lock-in Amplifier. Sensitivity settings used on the lock-in ranged from 20 mV to 500 μV and the typical time constant used was 300 msec. The output of the lock-in was sent to a MetraByte STA-16 DAS-16 accessory board matched to a MetraByte DAS-16 internal data acquisition board in a Zenith Data Systems Z248 computer. The data collection was controlled by Labtech Notebook software. The data was collected at 2 Hz for approximately 20 minutes, stored in ASCII format, and transferred to Origin software for generation of plots.

4.3   Experimental Procedure

4.3.1   Procedure Overview

Section 4.2 provided a description of the equipment used. This section tells how the samples were prepared, how the equipment was used, and what techniques were developed to produce the spectra presented in Chapter V. Detailed

procedures are presented in Appendix A and calibration techniques are presented in Appendix B.

4.3.2 Sample Preparation

The three $ZnGeP_2$ samples used in this study were provided by Dr. M.C. Ohmer of the Materials Directorate of Wright Laboratory. These samples, grown by the Bridgman method, (see section 3.2) include 11c which was ZnP_2 deficient, 13c which was near-stoiciometric, and 16c which was ZnP_2 rich. (28:54) All three samples had been annealed and bombarded with 1 MeV electrons to reduce the near band edge absorption. In addition, these samples have been previously studied by PL. (15) Samples 13c and 16c were square, approximately 1 cm on a side and 2 mm thick. Sample 11c was oval shaped, approximately 8 mm x 4 mm and 3 mm thick. The samples were taken from the fluoroware containers and mounted directly onto the sample holder. A small spot of rubber cement was placed on holder so that when the samples were put into position, only the top quarter or the sample came in contact with the rubber cement. After the rubber cement dried, the sample surface was swabbed with methanol to remove any dust. The samples were then loaded into the vacuum chamber which was evacuated to a pressure less than 5 x 10^{-7} torr.

4.3.3 System Preparation and Data Collection

After the chamber was evacuated, the samples were cooled by liquid helium, and the PMT was cooled by liquid nitrogen. After approximately twenty minutes, the temperatures of the sample and PMT had stabilized, the electronics were turned on and the software readied for acquisition. Next the electron gun was turned on, and the beam was positioned on the sample. The beam was positioned preferably on the bottom half of the sample since the top half of the sample holder was illuminated by filament glow. This area was avoided if at all possible so as to minimize background radiation from being collected along with the electron excited luminescence.

To locate the luminescence signal, the slits of the spectrometer were opened wide, the sensitivity of the lock-in set to the μV range, and the spectrometer set to the wavelength of a known peak. The lenses were translated and the beam position changed until a signal could be found. Once the signal was found, the phase was set between the lock-in and chopper, and the slits were closed to a typical width of 200 μm. In an iterative cycle, the sample was rotated, the lenses adjusted in all three dimensions, the beam position moved across the face of the sample, and beam focus adjusted until the signal was maximized. To insure that the signal was indeed the luminescence signal from the sample, the high voltage to the electron gun was switched off. With the high voltage off, the electrons were not

extracted from the gun and therefore not incident on the sample. However, the filament background did remain since the filament current was not affected. If the signal disappeared when the high voltage was off and reappeared when the voltage was on, it was assumed to be luminescence from the sample. After maximizing the signal and insuring its origin, the system was ready for data collection.

To begin the data collection process, the spectrometer was set 50 angstroms short of the desired starting wavelength. This insured that any backlash or slack in the gear mechanism of the spectrometer had been taken up by the time the desired starting wavelength was reached. The scan speed was adjusted to 226 angstroms per minute. Since this spectrometer was not programmable, a repeatable scan speed was obtained by setting the variable speed dial to the maximum position in the slow scan mode. The data collection rate was 2 Hz, so a data point was collected every 1.88 angstroms. Once the spectrometer had begun to scan at the desired wavelength, the data collection program was activated. The data acquisition was terminated after a programmed period of time. This time period was determined by dividing the total scan range by the scan speed. The data was stored to a floppy disk in ASCII format. After many spectra were taken, the raw data were read into a plotting program to produce hard copies.

4.4 Sources of Error

Data acquisition was initiated by pressing a key on the computer keyboard when the proper wavelength rolled by on the spectrometer counter. Because the coordination between the computer and spectrometer is not perfect, the intensity vs. wavelength calculation is undoubtedly in error ± 1 angstrom.

The scan speed of the spectrometer was not precisely reproducible; therefore, the time period need to collect data for the desired wavelength range was in error. As a result, the intensity vs. wavelength calculation is in error ± 0.1 angstroms

To reduce system errors, a calibration with a Krypton spectral line source was performed to verify the accuracy of the spectrometer. In addition, a calibration of the system response was performed using a blackbody source. Details of the calibrations are discussed in Appendix B.

4.5 Conclusion

Details of the experimental system were presented in this chapter. The equipment was described and its usage was explained. Further details are presented in Appendix A.

At this point, the background of this research project has been laid out. The basic theory needed to understand the source of the data has been presented and the means by which the data was acquired has been described. The data

obtained will be presented in Chapter V, and where possible
the phenomena observed will be explained.

V. Results and Discussion

5.1 Introduction

New CL data obtained on $ZnGeP_2$ as a result of this study are presented in this chapter. The basic approach was to observe one sample at a time, obtaining spectral data at optimum conditions for polarization state, temperature, beam voltage, and beam current. The parameters were then varied and new spectra taken to determine the effects of the changes. The most striking changes were seen when a linear polarizer was introduced, especially when its transmission axis was rotated about the optical path. The spectra shifted in energy and the polarization effects were quenched with increasing temperature. Only slight changes in intensity were noted when the beam parameters were varied.

5.2 Polarization Dependence

A great change in the spectral data was observed when a linear polarizer was introduced into the optical path. As expected and shown in Figure 20, the signal intensity decreased when an unpolarized beam passed through the polarizer. Notice though that the fundamental shape of the response was unchanged. All three $ZnGeP_2$ samples exhibit polarized CL. Figures 21-23 illustrate spectra taken when the transmission axis of the polarizer was oriented horizontally (P0), vertically (P90) and when no polarizer
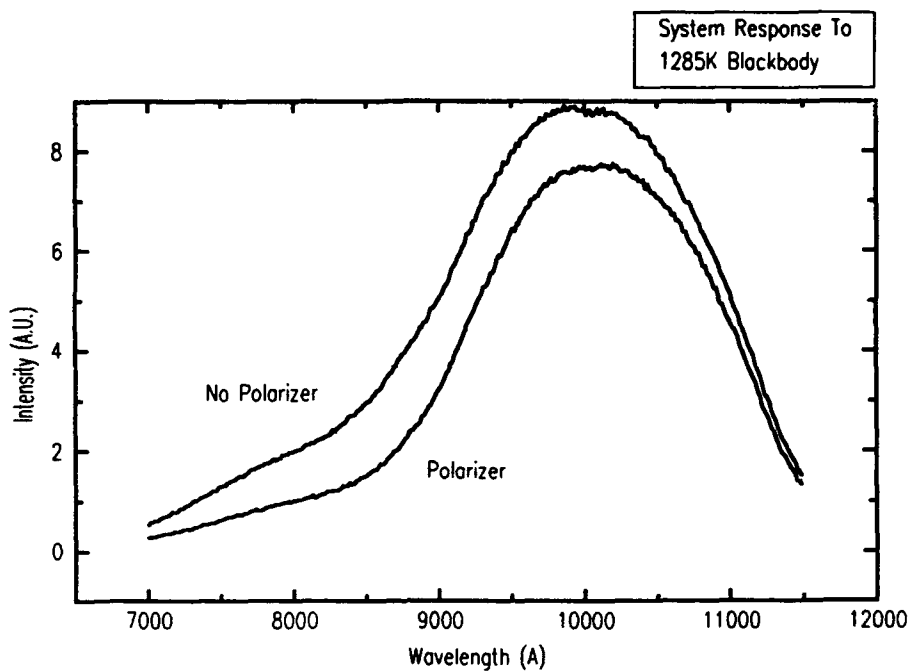
Figure 20. A plot of the system response to a 1285K blackbody source with and without a linear polarizer in the optical path between the source and the spectrometer.
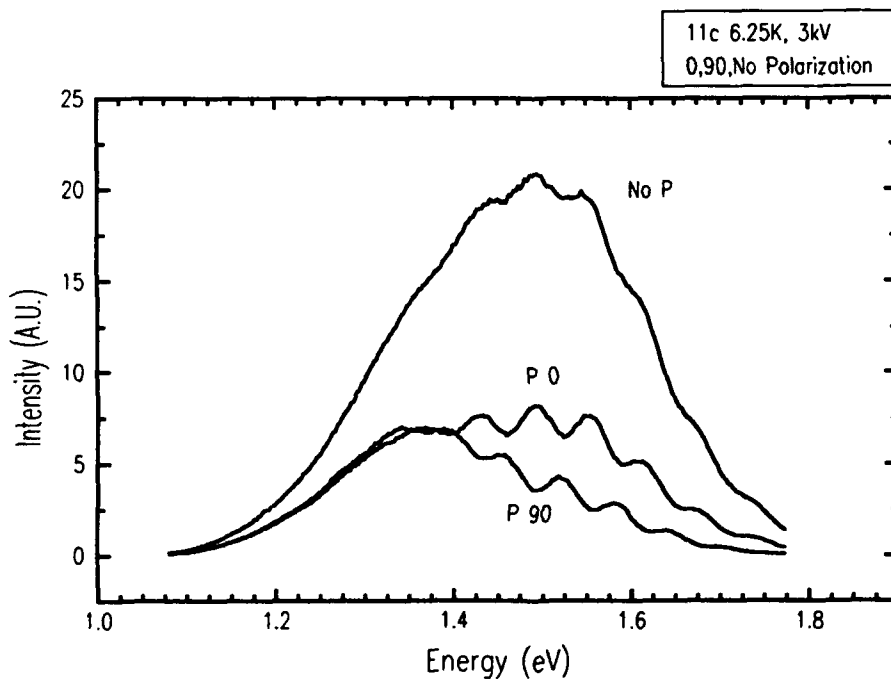
Figure 21. CL spectra of sample 11c showing intensity dependence on linear polarizer.
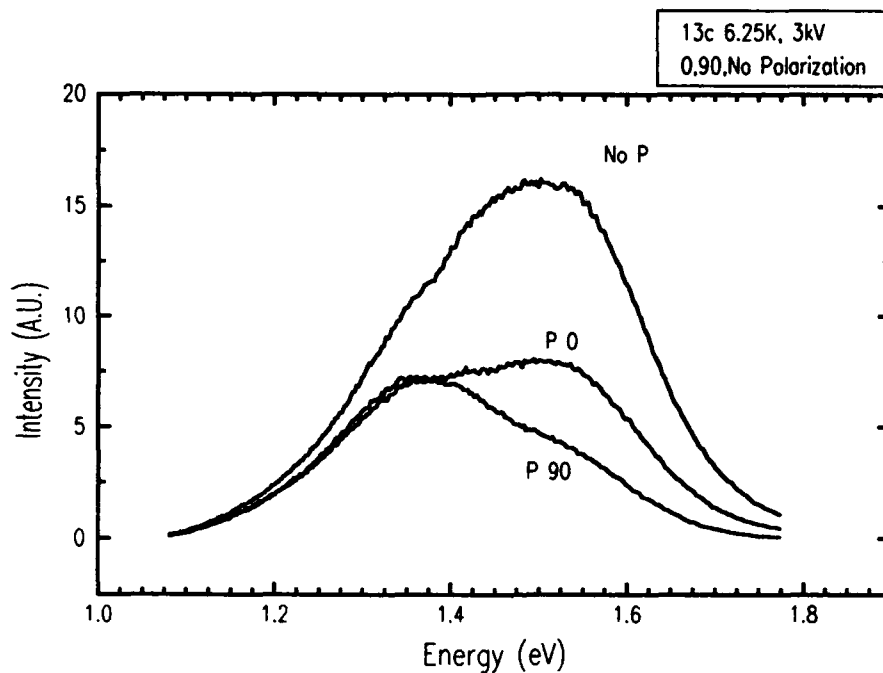
Figure 22. CL spectra of sample 13c showing intensity dependence on linear polarizer.
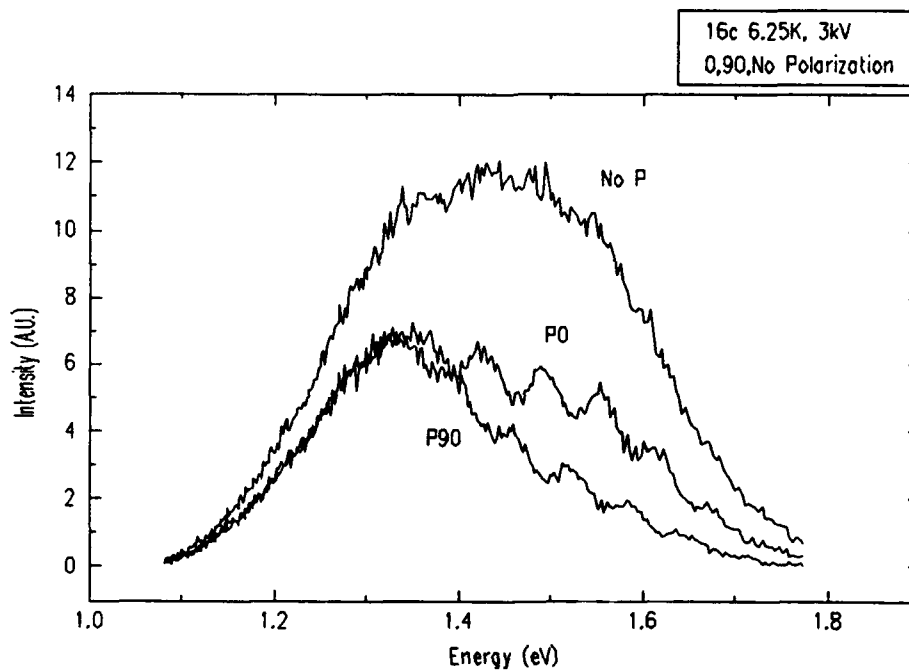
Figure 23. CL spectra of sample 16c showing intensity dependence on linear polarizer.

was present (No P). All three samples show a large peak at approximately 1.35 eV. This peak has been observed previously and has been determined to be associated with the acceptor level AL1 (1:453-457, 32:144-148). Since samples 11c and 16c exhibit structure not present in sample 13c, they were investigated further. At least seven smaller peaks, separated by energies of approximately 60 meV, emerge and appear to be riding on the large peak centered at approximately 1.35 eV. Figures 24-26 illustrate how the spectra change as the transmission axis of the polarizer is rotated around through 180 degrees. With increasing angle from the horizontal, the intensity decreases but the peaks stay aligned. After the intensity reaches a minimum at the vertical (P90) position, the intensity increases with increasing angle of rotation, and the peaks stay aligned. However, at the minimum, the peaks have shifted approximately 30 meV to lower energies. Figures 27-29 show the identical phenomena in sample 16c.
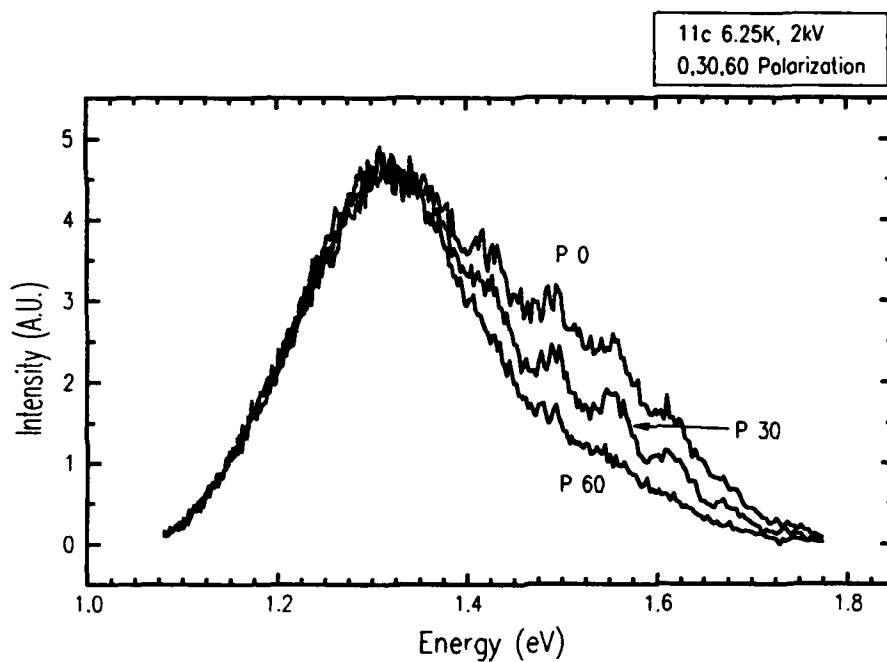
Figure 24.   CL spectra sample 11c at polarizer positions 0, 30, and 60.
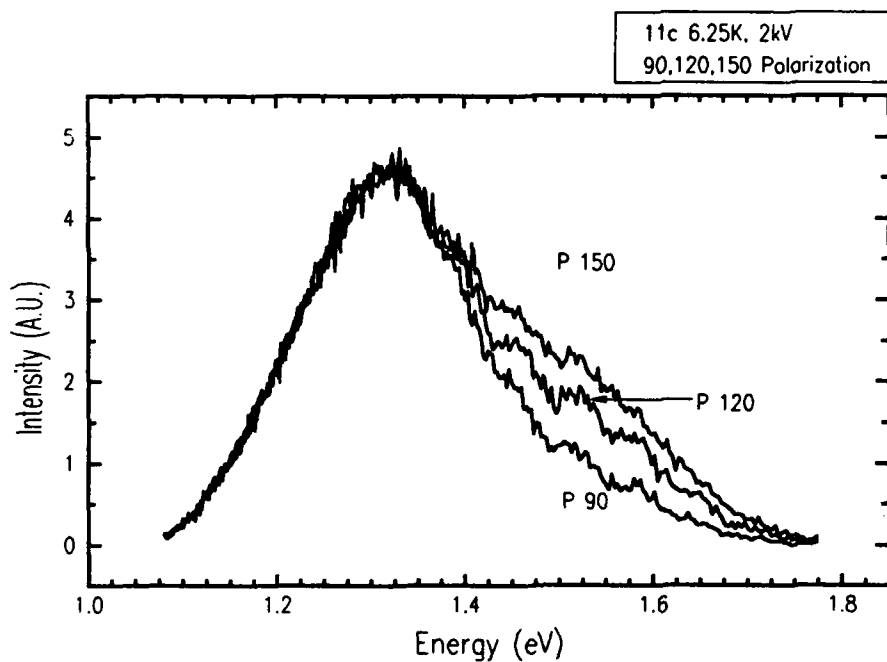
Figure 25.   CL spectra of sample 11c at polarizer positions 90, 120 and 150.
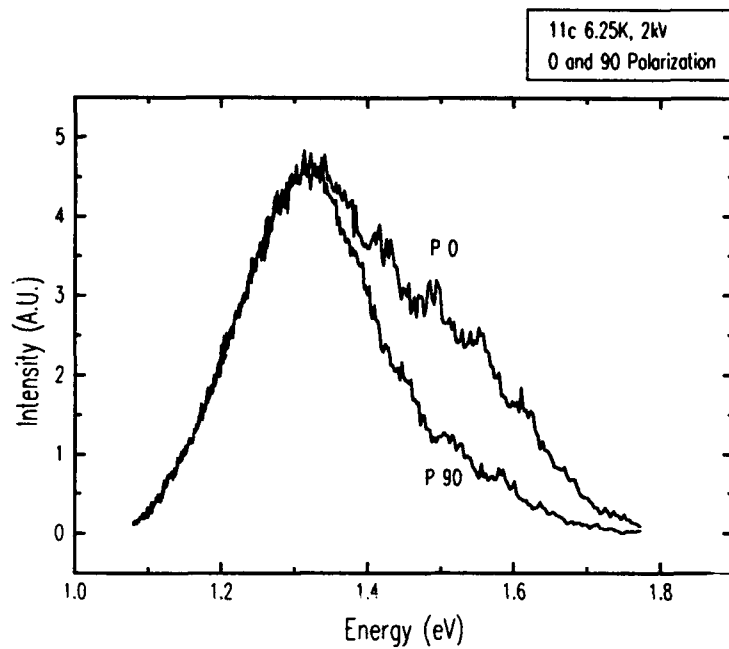
Figure 26. CL spectra of sample 11c at polarization positions 0 and 90, which show the maximum and minimum intensity levels.
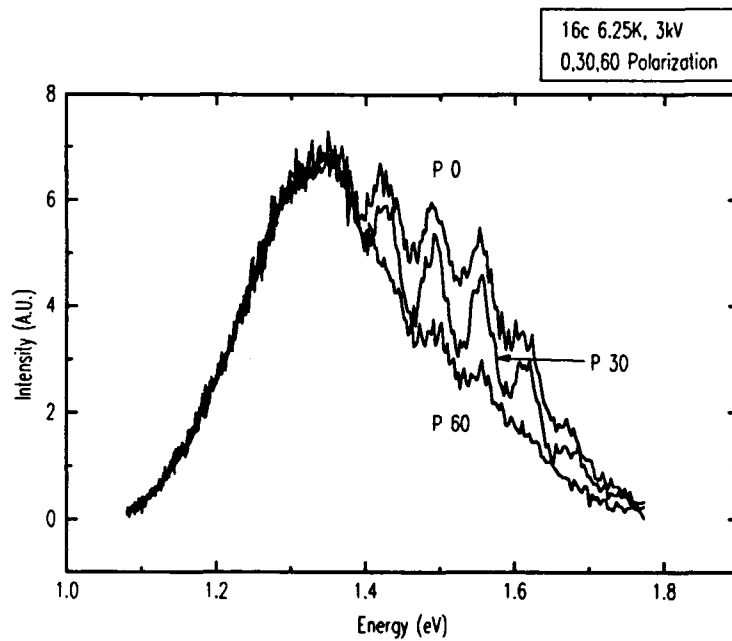
Figure 27. CL spectra of sample 16c at polarization positions 0, 30, and 60.
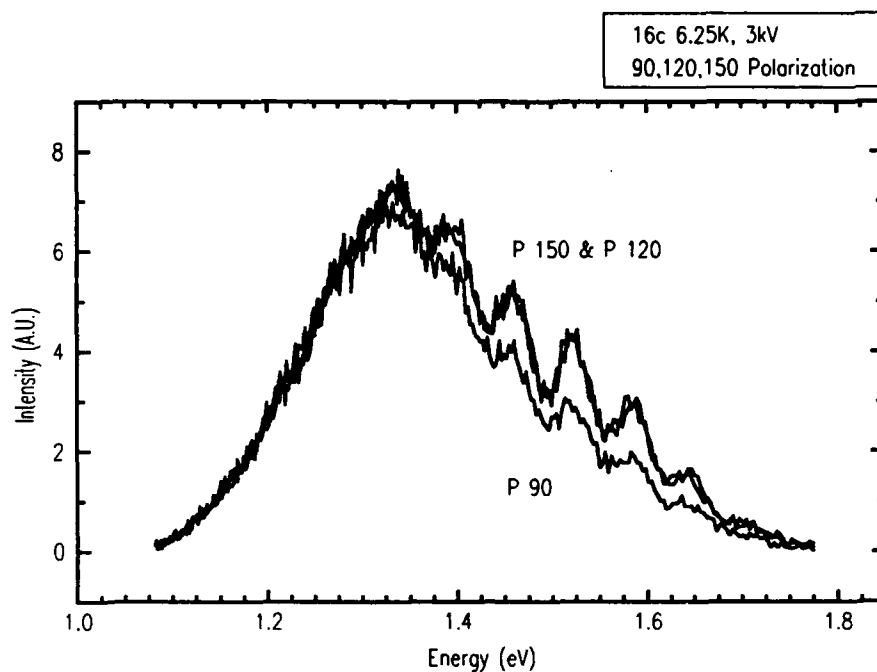
Figure 28. CL spectra of sample 16c at polarization positions 90, 120, and 150.
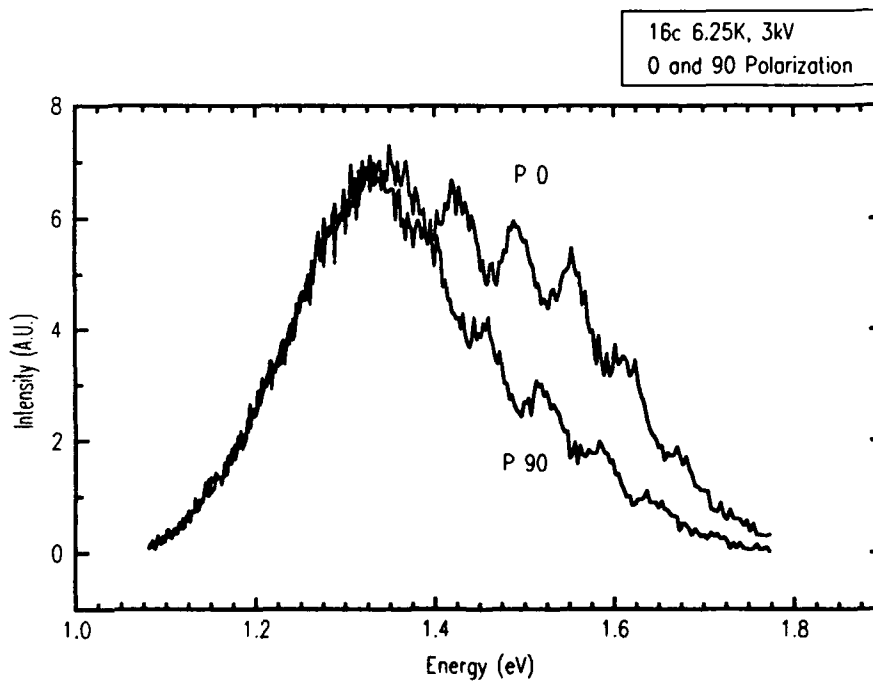
Figure 29. CL spectra of sample 16c at polarization positions 0 and 90 which show the maximum and minimum intensity levels.

5.3 Beam Parameter Dependence

The electron beam can be varied in two ways. Gun voltage can be changed, and thus the beam energy, to vary the depth of penetration into the sample. Gun current can be changed to vary the electron density, or the number of electrons striking the sample, and thus the intensity of the luminescence (see Section 4.2.3).

5.3.1 Beam Energy

A set of spectra were taken at different beam energies with constant gun current for all three samples. Figure 30 shows the voltage, or beam energy dependence for sample 11c.
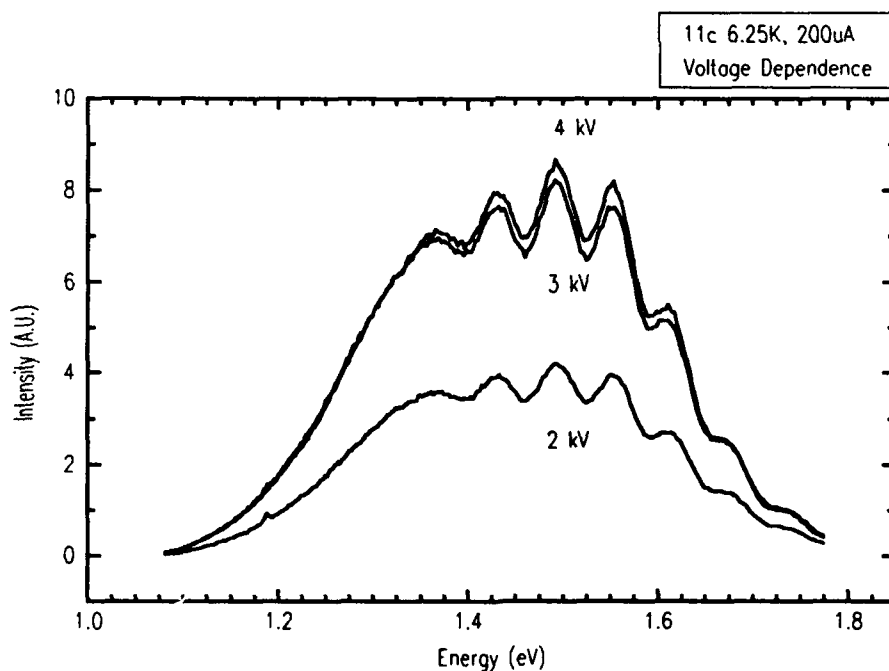
Figure 30. CL spectra of sample 11c showing intensity dependence on beam energy.

The spectra in Figure 31, also from sample 11c, were taken
at a different spot on the sample and at lower beam
energies. These spectra of sample 11c were taken with the
transmission axis of the polarizer oriented in the
horizontal position. As both figures show, the basic
structure is constant, but overall signal intensity is lost
with decreasing voltage.
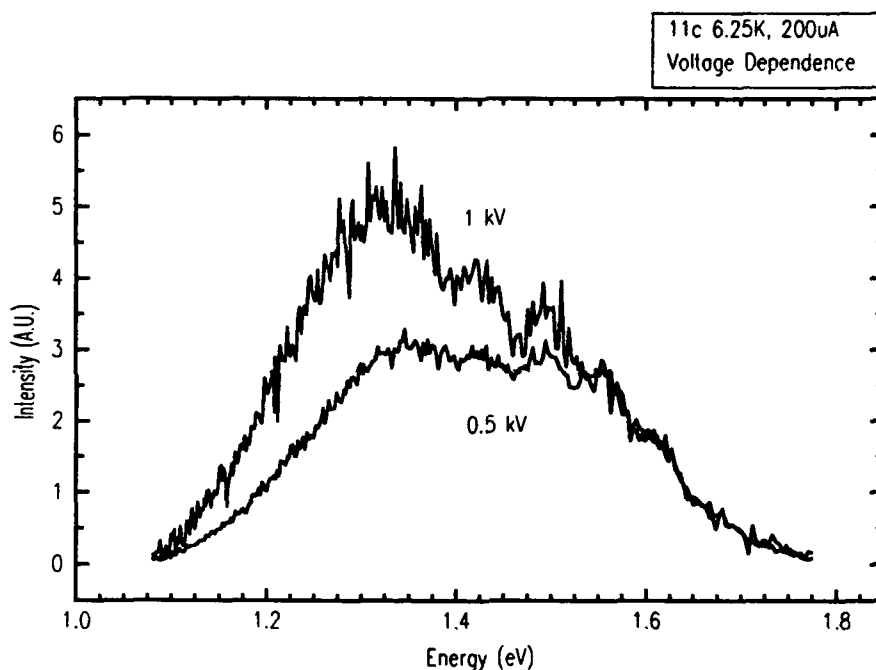
Figure 31.   CL spectra of sample 11c at
a different spot than in Figure 31 and at
lower beam energies.

Figure 32 shows a set of spectra for sample 13c. All data
were taken with no polarizer in place. Once again,
intensity decreases with decreasing voltage, but the line
shape stays the same.
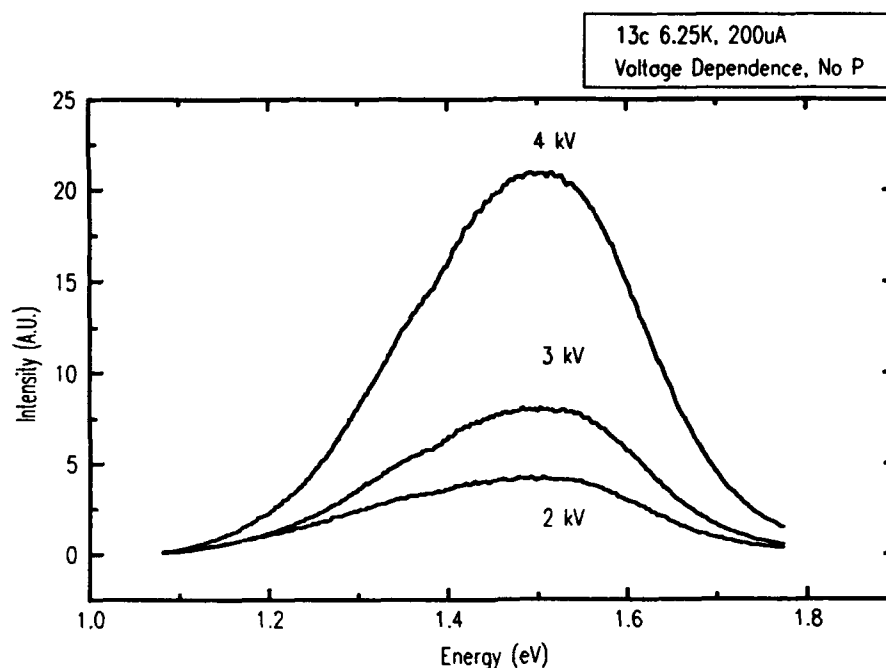
Figure 32. CL spectra of sample 13c showing
intensity dependence on beam energy.

The voltage dependence data for sample 16c is presented in
Figure 33. The transmission axis of the polarizer was
rotated 30 degrees from the horizontal for this data set.
The same trend is observed; signal intensity decreases with
decreasing beam energy but maintains a constant shape. The
fact that the line shape is constant for different beam
energies would indicate that the crystal is homogeneous and
therefore has a constant composition over the range
penetrated by the electrons, 300 to 8000 angstroms (see
Appendix C).
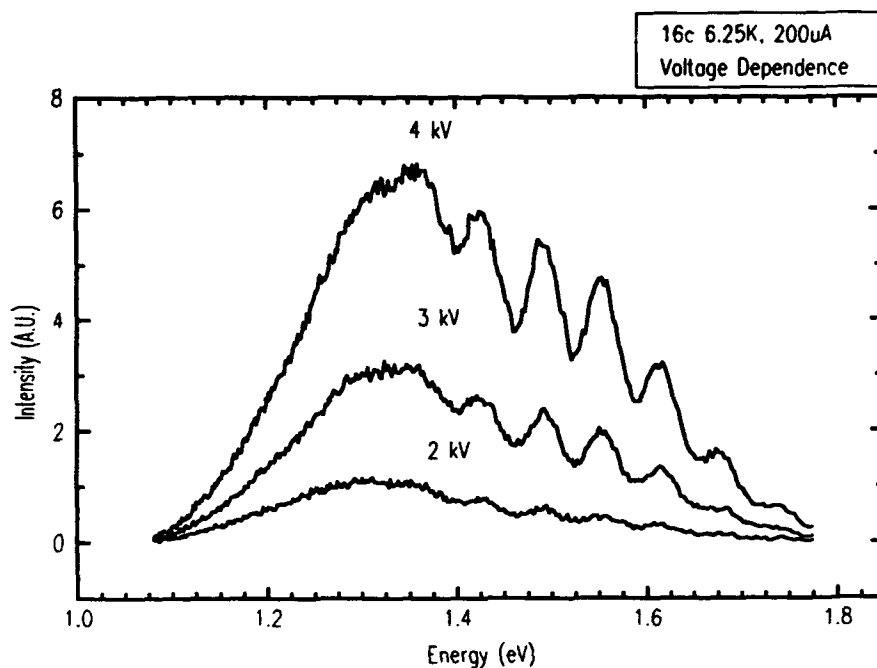
Figure 33. CL spectra of sample 16c showing intensity dependence on beam energy.

5.3.2 Beam Current

A set of spectra were taken with constant beam energy and three different beam currents for two of the samples. Data taken on sample 11c are shown in Figure 34. The spectrum at 200 mA was taken at a different spot on the sample than those at 100 and 50 mA; however, one notes that the signal intensity decreases with decreasing gun current. This is logical since lower beam currents decrease the number of excitation electrons impinging on the surface of the electron beam, and as a result, fewer electron-hole pairs are generated. The same trend is observed in the spectral data taken on sample 16c presented in Figure 35.
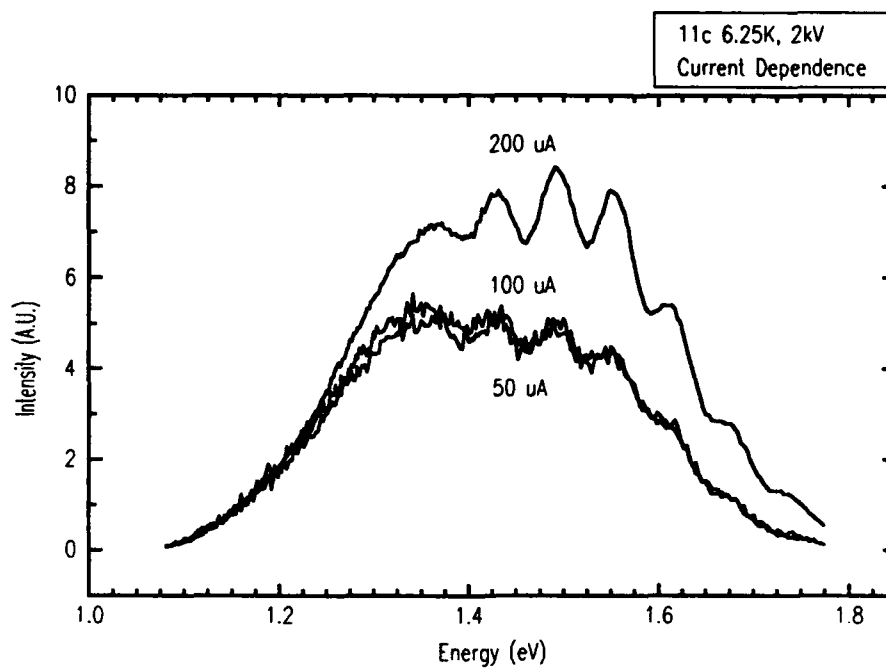
Figure 34. CL spectra of sample 11c showing intensity dependence on beam current.
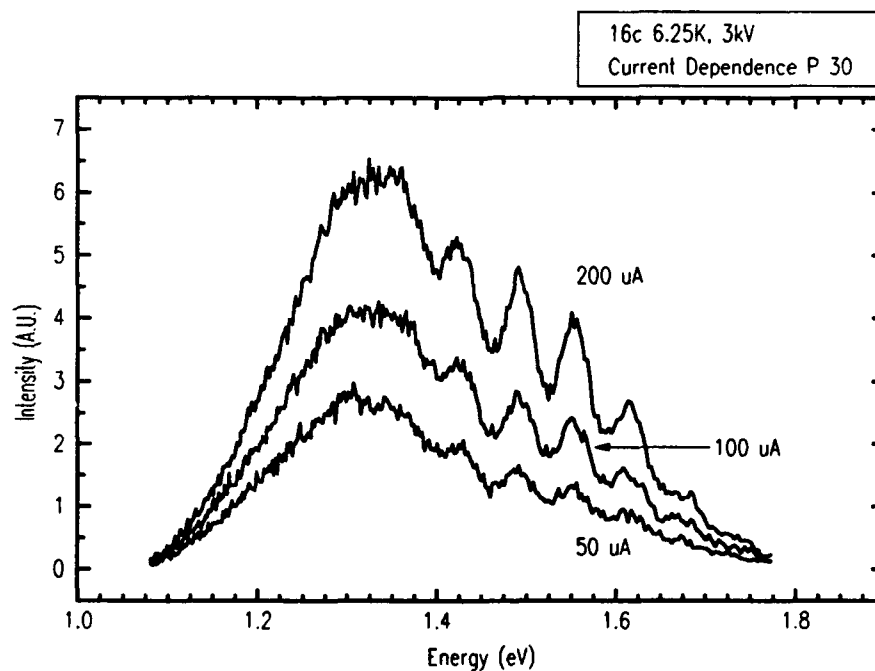
Figure 35. CL spectra of sample 16c showing intensity dependence on beam current.

This data confirms the idea of sample homogeneity proposed as an interpretation of the beam energy data. Other than intensity, the spectral output of the samples does not change with variations in the electron beam.

5.4 Temperature Dependence

As a general rule, luminescence data is taken at the lowest possible temperatures to obtain as much fine structure in the spectra as possible. Linewidths narrow and intensity increases with decreasing temperature since the effects of thermal broadening are minimized. Furthermore, collecting data at various temperatures can help in the analysis of a spectrum. For example, since excitons are observed only at very low temperatures, a peak attributed to an exciton should disappear with increasing temperature.

Figures 36 and 37 illustrate the spectra of sample 11c taken at various temperatures. In addition, the angle of the analyzer has been varied; i.e. the luminescence in Figure 36 is polarized horizontally and covers a small temperature range whereas the luminescence in Figure 37 is polarized vertically and covers a much larger temperature range. It can be noted that the intensity of the multiple peak structure decreases much faster for luminescence analyzed through a vertical polarizer than the 1.35 eV AL1 peak such that by 70K, the multiple peak structure is not noticeable.
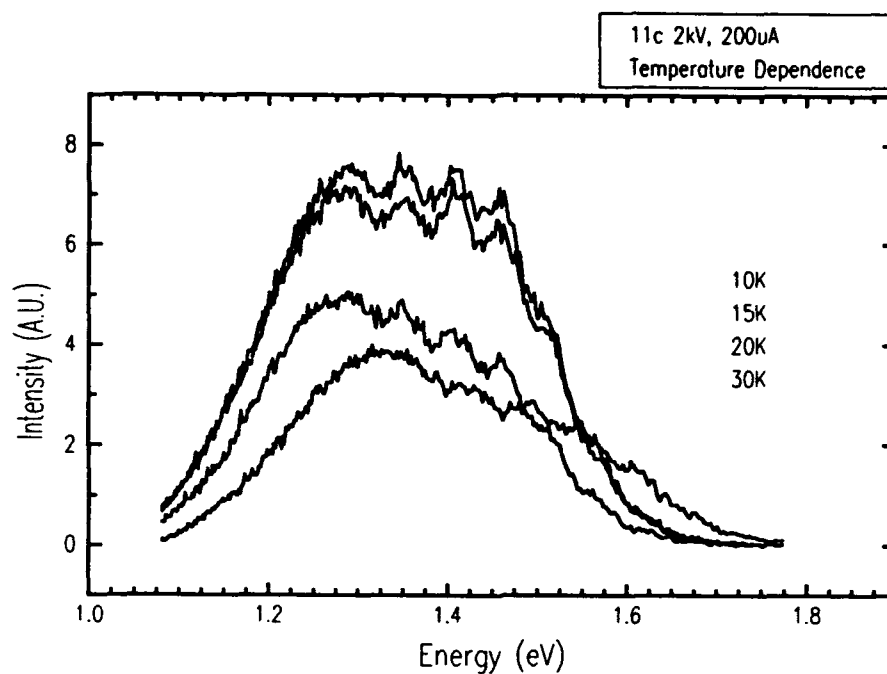
Figure 36. CL spectra of sample 11c showing intensity dependence on temperature, polarizer at position 0.
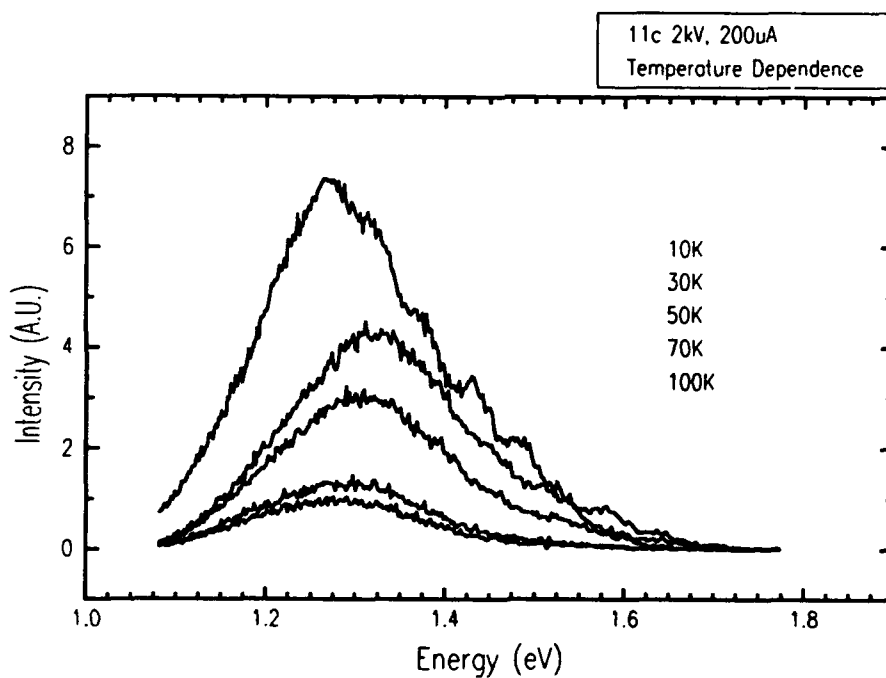
Figure 37. CL spectra of sample 11c showing intensity dependence on temperature, polarizer at position 90.

Figure 38 is a temperature dependent plot for sample 16c at polarizer position 90. Although the overall intensity decreases with temperature like the spectrum of sample 11c, the multiple peak structure is still visible at 100K. The implications of this temperature data is not obvious. A study of more samples is necessary to better define temperature effects.
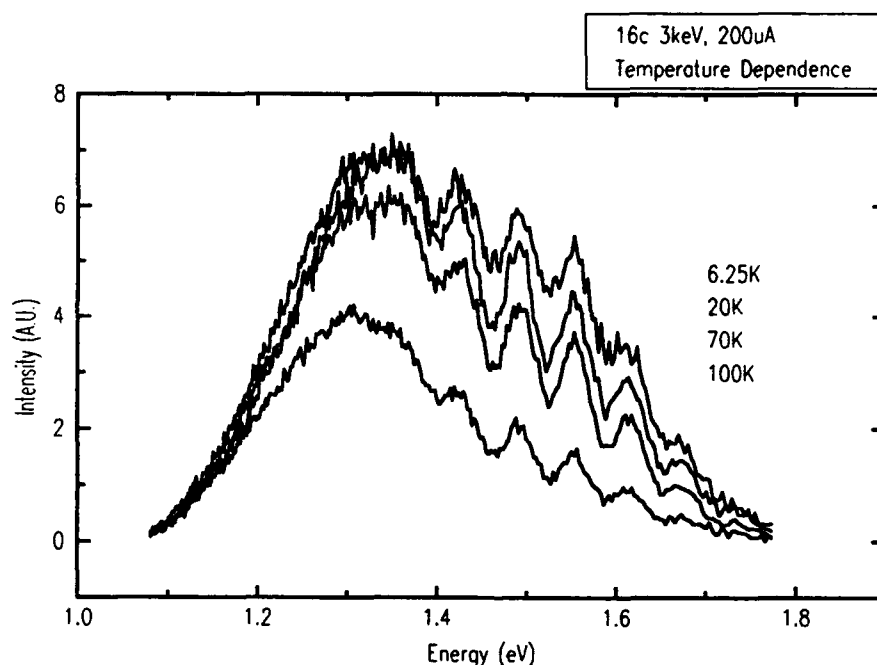
Figure 38. CL spectra of sample 16c showing intensity dependence on temperature, polarizer at position 90.

5.5 Discussion

The data presented shows that $ZnGeP_2$ has more structure in its luminescent spectrum than has been previously reported. At least seven peaks in addition to the peak

associated with AL1 are clearly evident. These peaks are separated by 60 meV and are polarization and temperature dependent. The reason for the emergence for these peaks is not clear, however some possibilities can be eliminated.

5.5.1 Phonon Replicas

One possibility is that these peaks, which are equally spaced in energy, are phonon replicas of the large peak at 1.35 eV. As indicated in Section 2.3.3, phonon replicas are indeed separated by equal energies hw , but they would occur on the lower energy side of a sharp transition as indicated in Equation 12

$$hu = E_g - E_r - nhw . \qquad (12)$$

The small peaks exhibited in samples 11c and 16c are on the higher energy side and thus cannot be phonon replicas.

5.5.2 Excitonic Transitions

A second possibility is exitonic transitions. Exitonic transitions should be observed on the low energy side of band edge transition as expressed in the following equations:

$$hu = E_g - E_{ex} \qquad (7)$$

and

$$hu = E_g - E_{ex} - E_b. \qquad (8)$$

Energy levels of an exciton are not equally spaced as was
indicated from the hydrogen model used to approximate the
energy levels (Section 2.3.3). Yet the peaks in the spectra
of 11c and 16c are equally spaced. Furthermore, the seven
small peaks are evident in sample 16c even at 100K, a
temperature much too high to see exciton transitions of this
magnitude. One can thus conclude that these observed peaks
are not associated with excitons.

5.5.3 Impurities

Impurities often introduce new energy levels into the
band structure. As previously discussed in Section 2.3.3,
electron-hole recombination can occur via acceptor and donor
levels. The samples used in this study were analyzed for
impurities by spark source mass spectography. The
measurements indicated concentrations less than 1 ppma. (16)
These concentrations are 1000 times less than the AL1
concentration. Therefore the multiple peak structure is not
believed to be due to impurity states.

5.5.4 DAP Transitions

Just as phonon replicas and excitonic transitions can be
eliminated as sources of the seven peak structure seen in
samples 11c and 16c, donor-acceptor-pair transitions (DAP)
can also be eliminated.

The DAP theory suffers from the same malady as the
phonon replica theory, i.e. DAP transitions between donors

and AL1 should be evident on the lower energy side of the free-to-bound peak known to exist at approximately 1.35 eV. The peaks in the spectra of samples 11c and 16c are on the high energy side. In addition, from equation 11, the energy of the recombination emission depends of pair separation

$$hu = E_g - E_a - E_d + \frac{q^2}{er}. \qquad (11)$$

A transition between distant pairs is less probable than a transition between nearer pairs; therefore, the emission intensity should increase as the pair separation decreases or hn increases. As observed in Figure 33, the peak intensities appears to increase with decreasing energy. Furthermore, at large values of r (r > 40A) the emission lines overlap, forming a broad spectrum. (27: 143) By reexamining Figure 33, one can note that the distance between adjacent peaks remains somewhat constant and no overlapping is observed. Therefore, these peaks cannot be due to DAP transitions.

5.5.5 Electron Bombardment Damage

All three samples were bombarded with high energy electrons after growth but before this study. It is possible to conceive that the damage to the lattice caused by the irradiation may have introduced energy levels into the band gap. However, the multiple peak structure is

present in only two of the three irradiated samples. As a result, lattice damage can be discounted in this case.

5.6 Excitation Mechanism

Thus far, in quest to determine the origin of the seven peak structure evident in the spectra of samples 11c and 16c, but not evident in the spectrum of sample 13c, a few possibilities have been eliminated. These possibilities have been associated with the properties of the crystal. Perhaps the phenomena is an artifact of the CL system; however, if the seven peak structure was an artifact of the system itself, all three samples should exhibit the same behavior.

As previously described (see section 4.2.1), the chamber used to perform CL measurements could also be used to perform PL measurements. To determine if any differences in spectra resulted when the crystal was excited by different means, a sample CL spectrum was taken at 6.25K, 3 kV, 200mA. Then without changing anything else, the sample was rotated so that an argon ion laser, at 488 nm with 30 mW of incident power excited luminescence, and another spectrum was taken. A comparison of the spectral data is presented in Figure 39. The spikes evident on the PL spectrum are emission peaks in the Argon plasma.
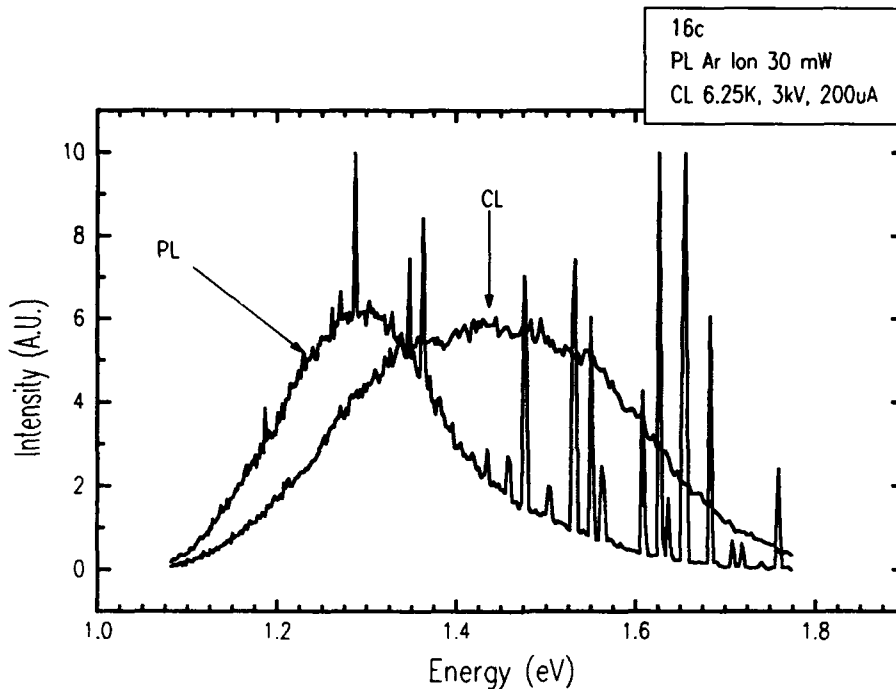
Figure 39. CL and PL spectra of sample 16c
taken under identical conditions.

A comparison of the non-polarized CL data with the PL data
shows a great difference in line shape. The reason for the
difference in CL and PL spectra has not been firmly
established; however, a few factors must be considered. As
previously mentioned, differences may arise due to
differences in sampling depth. Further more, the electron
beam is completely unpolarized while the laser is generally
linearly polarized.

5.7 Proposed Model

Several possible explanations for the emergence of
peaks not directly attributable to AL1 were discussed:
phonon replicas, transitions involving excitons, DAPs and

impurity level transitions, and electron bombardment damage. However, all of the aforementioned possibilities are not consistent with the observed data. Dr. Mel Ohmer of the Materials Directorate of Wright Laboratory has suggested a possible explanation. In his model, it is proposed that the peaks 1-3 in Figure 40 are transitions between Γ_3 ($\Gamma 7$ with spin orbit splitting) in the conduction band and AL1, which reflects the crystal field and spin orbit splitting of Γ_4 and Γ_5 in the valence band ($\Gamma 7$ and $\Gamma 6$, $\Gamma 7$ with spin orbit splitting). Refer to Figures 13, 14 and 41. It has been reported by Sheleika (30:85) that Δ_{cf} is 94 meV and Δ_{so} is approximately 63 meV. Since the peak separation between successive peaks in Figure 40 is 58 to 66 meV, this data suggests that the combined effect of crystal field and spin orbit splitting results in an energy separation of approximately 60 meV between the triplet states in the valence band. This model also suggests that peaks 4-6 are either transitions between Γ_2 and AL1 or transitions between Γ_3 and another acceptor level 0.56 eV up from the valence band. Peak 7 is possibly a transition between Γ_1 and the highest triplet state in AL1. Other transitions to the triplet may be weak and therefore not easily detectable.

These transitions have not been previously observed. Perhaps their emergence is an artifact of the high degree of crystalline quality of the samples studied. Since the CL spectra differed dramatically from previously reported PL data (15), it appears that the excitation mechanism plays
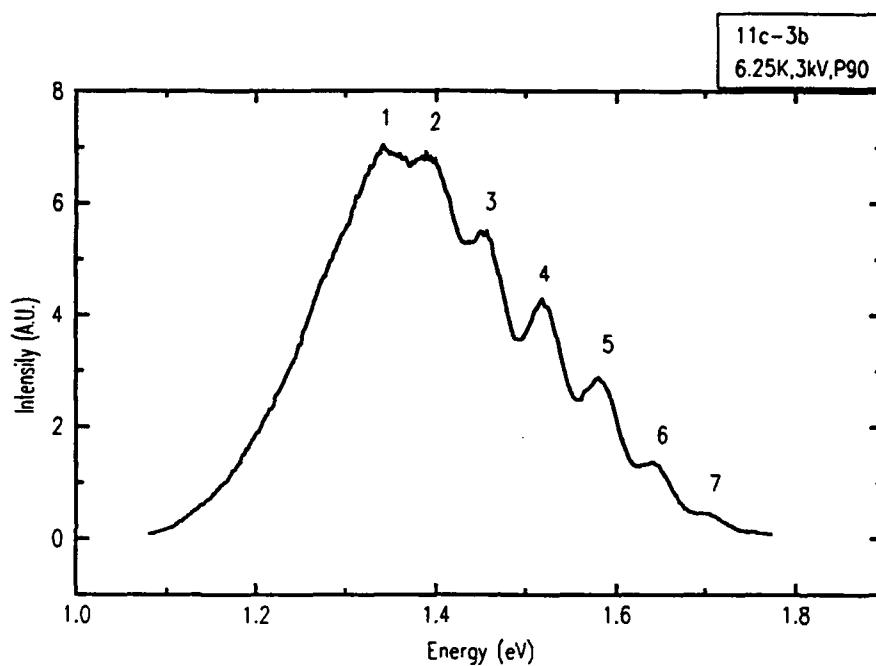
Figure 40. CL spectra of sample 11c showing possible transitions at the Γ point in the Brillouin zone.
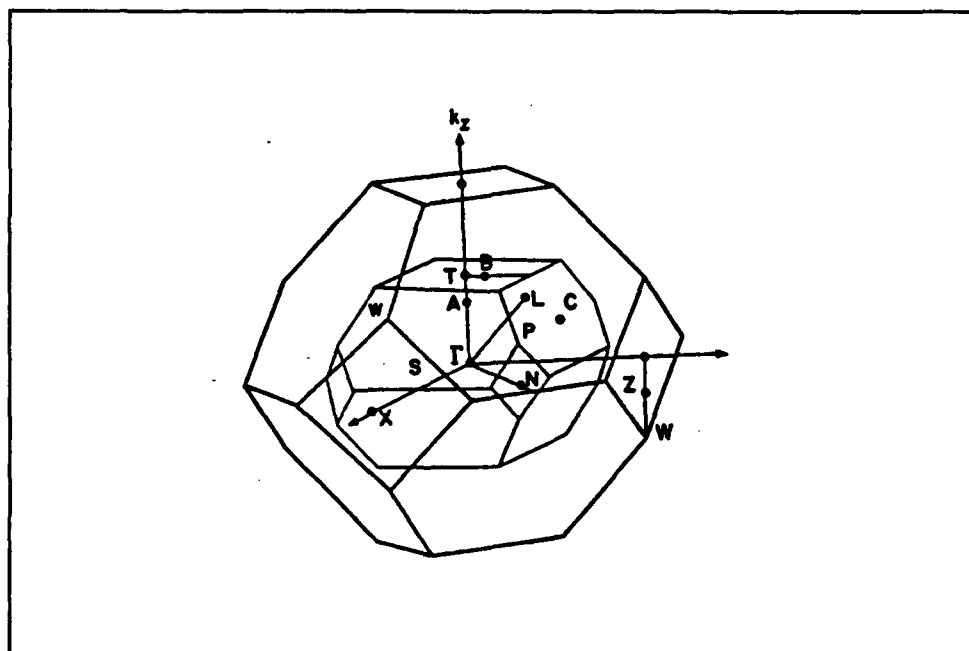
Figure 41. Comparison of the Brillouin zones of the zincblende and chalcopyrite lattices. (30:80)

some role in the emergence of these peaks.

At this point, the details of the polarized response are not yet clear. Recommendations for further research that will help develop a more complete picture are presented in the next chapter.

VI. Conclusions and Recommendations

6.1 Final Conclusions

A partial set of the spectral data collected in this study has been presented. The data was obtained under various conditions of electron beam energy, beam current, sample temperature, and luminescence polarization state. Such CL data on $ZnGeP_2$ is believed to be presented here for the first time. It has been observed that the line shape of the spectra was not altered by changing the electron beam parameters, leading to a conclusion that the samples were homogeneous in composition.

The temperature dependence data is not conclusive. Sample 11c showed a temperature dependence such that all the peaks, except the one associated with AL1, were quenched at 70K. However, sample 16c showed very little temperature dependence. All the structure remained evident to at least 100K.

The polarization state dependence is clearly the most intriguing. All three samples exhibited different spectra with regard to changing polarization state. This phenomena is undoubtedly due to the birefringent nature of the crystal. However, samples 11c and 16c exhibit a multiple peak structure, not previously observed in previous $ZnGeP_2$ luminescence data, which cannot be as birefringence phenomena. It is believed that these peaks are evidence of

the triplet state in the valence band induced by crystal field and spin orbit splitting.

6.3   Recommendations

In order to make a better determination of the multiple peak structure, more studies must performed. The most obvious extension of this study would be to look at more samples.   A study on samples where the c-axis is definitively known may prove advantageous to determining the effects of polarized input and the polarization of the spectral output. A half-wave plate may be used to vary the angle between the c axis and the electric field vector of an incoming laser beam.

A number of other measurements may determine the nature of the energy levels in the forbidden band gap. Time-resolved CL, selective sub band-gap excitation, and electron reflectance are viable options.

It may prove interesting to look at un-radiated samples. This is the most obvious way to determine the effects of radiation damage.

Appendix A

This appendix will detail operating procedures for the cathodoluminescence system.

Glossary Of Abbreviations

CL - Cathodoluminescence

$\Delta\lambda$ - Delta Lambda (wavelength)

FWHM - Full Width Half Maximum

He - Dry Helium

N_2 - Dry Nitrogen

IP - Ion Pump

LHe - Liquid Helium

LN_2 - Liquid Nitrogen

PL - Photoluminescence

TC - Thermocouple

TSP - Titanium Sublimation Pump

Safety Information

High Voltage

High voltages, up to 5kV, are necessary to operate the electron gun. High voltage is also present in the vac-ion pump. When opening the power supply, unplug from the outlet and allow 30 minutes for the capacitors to drain and then discharge the capacitors before handling the internal components. Make sure that the grounding cable is securely attached to the chamber and that the chamber itself is properly grounded. When testing voltages on the high voltage cable, use the high voltage probe and appropriate

rubber gloves. Check periodically to insure that all cables
are properly secure.

Cryogenics

Liquid helium and liquid nitrogen pose potential
safety hazards in the form of frostbite. Use gloves and
protective eye wear when transferring nitrogen from the
large storage dewar to the smaller dewar. In addition, use
gloves when removing the Helitran cold end above the liquid
helium level or when changing helium dewars. If the flow
rate through the Helitran shield is high, a large amount of
frost will form of the exhaust line. Take care to avoid
condensation or melting frost that will drop on electrical
components.

Power Failure

No danger exists in the case of power failure. Upon return
to power, insure that the ion pump is in the start mode
until the appropriate pressure level has been reached. If
the power is off for an extended time, stop the helium flow
and remove the cold end from the LHe. This action is to
prevent an ice block at the cold finger vent since the
heater will be off.

Solvents

The samples and sample holder are cleaned with
methanol. Avoid prolonged exposure or ingestion.

Pump System

Pump Down Procedures

- Start the roughing pump and observe the thermocouple (TC) gauge. When pressure falls below 100 microns, turn on turbo pump.

- Turn on ionization gauge. When pressure falls to 10^{-5} scale, turn on the Vac-Ion (IP) in the start mode.

- If Vac-Ion starts, then close valve to main chamber.

- Start the sublimation pump (TSP) and run the timer to 100% and filament to 50 A. Switch the ion pump (IP) to start position (this overrides the protect circuit) and observe the TC gauge. If the pressure starts to rise, turn off IP for 1 minute, otherwise, run the pump for 2 minutes then switch off for 1 minute. When the current on the IP falls below .4A, switch to protect mode.

- When pressure reads on scale, ease TSP back to 20%.

- Continue to toggle IP on and off until pressure reads on mid 10^{-6} scale.

Vent Procedures

- Make sure that the IP and power supply for the gun are off.

- Attach the hose from the dry N_2 to gas inlet and open the pressure regulator. Set the regulator to a few PSI.

- Open the valve to the gas inlet, and open the main valve to the chamber.

- Allow enough time for the chamber (approximately 2 to 5 minutes depending on the flow through the regulator) to completely backfill before opening the chamber to the atmosphere.
- Maintain a small flow while the system is open to the atmosphere to insure the highest ambient purity possible in the chamber. Turn off the flow after replacing the sample holder and sealing all other ports.

Sample Preparation

Mounting

- Clean the copper block with a cotton swab and Methanol.
- Dab a small amount of rubber cement on the back side of the sample.
- Place the sample on the copper block and press lightly with the swab.
- Allow 2 to 3 minutes for rubber cement to dry.

Cleaning

- The samples under investigation have been received in a relatively clean state. After mounting the samples on the copper block, swab lightly with methanol to remove any rubber cement that may have gotten onto the surface.

Spectrometer

Alignment

- Remove any detector that may be present on the exit port.
- Remove lid from spectrometer.
- Position light source (preferably a laser) along the optical path. Reflect the source off the sample or a place as close as possible to the position the sample will occupy.
- Focus the light onto the entrance slit.
- Place a white target on the first mirror.
- Level and rotate the spectrometer until the incoming light is centered on the target.
- Position grating at proper wavelength so that incoming light reflects onto second mirror.
- Place the target on the second mirror and fine tune the leveling and rotation so that light is centered on target.
- Re-adjust until light is centered on both mirrors.
- Check to see that light is now exiting through the center of the exit slit.
- Secure the legs on the spectrometer (epoxy if appropriate).
- Replace lid.

Calibration

- Mount a spectral source (Kr, Ne, Hg, Xe, Ar lamp) in front of the entrance slit.

- Scan the spectrometer with both slits open to 500 μm.

- Close the slits to a minimum (approximately 10 to 20 μm) after positively identifying a particular line. Scan over the wavelength range to be calibrated and determine average $\Delta\lambda$.

- Close exit shutter and exit slit to protect the detector, then open the spectrometer and adjust the calibration knobs on the grating.

- Open the shutter and slit and re-scan the wavelength range to determine $\Delta\lambda$.

- Repeat grating adjustment until $\Delta\lambda$ is adequate.

Blackbody Correction

- Obtain a blackbody source and position it so that the output is incident on the entrance slit.

- Scan the spectrometer over response range of detector or a smaller subset if appropriate and store the data.

Correction over an entire range

- Find the ratio of the first point in the data file to every other point (normalize).

- Find a similar set of ratios for a true blackbody over the same wavelength interval.

- Divide the blackbody ratio by the collected data ratio.
- Multiply subsequent data sets by this correction factor to obtain data corrected for system response.

Correction over a subset

- Find a curve fit to the original system response over the desired wavelength interval.
- Generate a data set using the fit, and find the ratio of the first point to every other point (normalize).
- Find a similar set of ratios for a true blackbody over same wavelength interval.
- Divide the blackbody ratio by the collected data ratio.
- Multiply subsequent data sets by this correction factor to obtain data corrected for system response.

Data Collection

Spectrometer

- Set the desired scan speed by adjusting the appropriate knob on the spectrometer controller. Time with a stopwatch to get an accurate measurement.
- Scan the spectrometer in the same direction every time for data acquisition. Begin scan at least 50 angstroms before desired starting wavelength.
- Never allow the spectrometer to reach the end of its travel. This will cause the grating to shift and re calibration may be necessary.

Setup

- Turn on power to all equipment.

- Open slits wide and set sensitivity of amplifier to 100 mV or more.

- Place excitation beam on the sample. Manipulate the sample, lenses, or beam until a signal is detectable.

- Once signal is detectable, set the phase angle on the lock-in amplifier.

- If signal is too large, begin to close the slits and increase the sensitivity.

- Set the desired beam characteristics: filament current, gun current, electron energy.

- Begin maximization process by adjusting sample position, beam position, beam focus, lens position (vertical, parallel, and perpendicular to beam direction), and detector position (where appropriate) in an iterative manner.

- Continue to close slits and increase sensitivity as necessary.

Software

- Install proper data acquisition software. This study used Labtech Notebook. See the manual for further information.

- Once the system has been configured (see installation manual), very few parameters must be changed. Determine, from the scan speed previously set and the desired

84

wavelength interval, the time necessary to complete a scan. Enter this information in the Options and Setup Menus.

- Under the Files sub menu of the Setup menu, specify the filename for the data set. File header information may be added in this sub menu as well.

- Set the CRT display characteristics under the Display sub menu of the Setup menu.

- Executing the GO command from the main menu will initiate the acquisition process. An additional keystroke of any kind may be necessary depending on conditions specified while configuring.

- Store the data to floppy disks for further analysis later.

Documentation

- Record all settings, electron gun, spectrometer, amplifier, filename, etc., in a lab notebook.

- Record observation of anything out of the ordinary during acquisition run.

Miscellaneous

Detectors

- Never apply high voltage to a warm detector. Allow at least 15 minutes after filling detector dewar before powering up.

- Top off the dewar again after 2 hours, or in the case of the PMT, ensure that the LN_2 supply is adequate.

- Never expose cooled detector to room light. In case of the Ge detector, allow it to reach room temperature before removing or installing.

Temperature Fluctuations

- Watch for temperature or pressure fluctuations. Increase LHe flow through the tip if necessary.

Appendix B

This appendix describes the calibration process
performed to correct for system response in greater detail.
Wavelength calibration via spectral lines is also reported.

The grating response is not linear vs. wavelength. It
was designed to provide maximum response at 1 micron. The
PMT is also nonlinear. It does however follow a typical S1
response curve. To correct the spectral data for the
combined system response, a blackbody calibration is
performed.

An Electro-Optic Industries blackbody source was used
for the calibration. The temperature used was 1285 K, the
maximum temperature obtainable from this source. The output
of the blackbody was reflected off a front reflecting mirror
into the entrance slit of the spectrometer. A spectra was
taken just as if the blackbody light was the luminescent
signal from a sample.

The ideal blackbody data can be found by using the
Plank radiation law

$$L_\lambda = \frac{2\,hc^2}{\lambda^5} \frac{1}{e^{\frac{hc}{\lambda KT}} - 1} \tag{17}$$

where L_λ is the spectral radiance. (5:55) To obtain a
spectrum corrected for the system response, take the

following steps: 1) normalize both sets of data 2) divide
blackbody data at a particular wavelength by system response
data at the same wavelength to obtain correction factor 3)
multiply subsequent data sets by the correction factor at a
given wavelength. Corrected and uncorrected data are shown
in Figure 42.

The wavelength counter of the spectrometer must be
calibrated by a spectral source to insure that the intensity
vs. wavelength measurement is accurate. If the spectrometer
is moved, or the grating is changed, the calibration must be
repeated. To perform a wavelength calibration, take
following steps: 1) place a spectral source (Kr, Hg, Ar,
vapor lamp) in front of the entrance slit 2) match
wavelengths of known peaks (from CRC) to the peaks found by
the spectrometer 3) in an iterative cycle, adjust grating to
align the peaks and re-scan the spectrometer. After
adjusting the grating, the spectrometer must be scanned back
from the peak at least 100 angstroms before the peak
position is found again. This process will insure that the
slack is taken out of the gear mechanism. A spectrum of a
krypton lamp is shown in Figure 43.
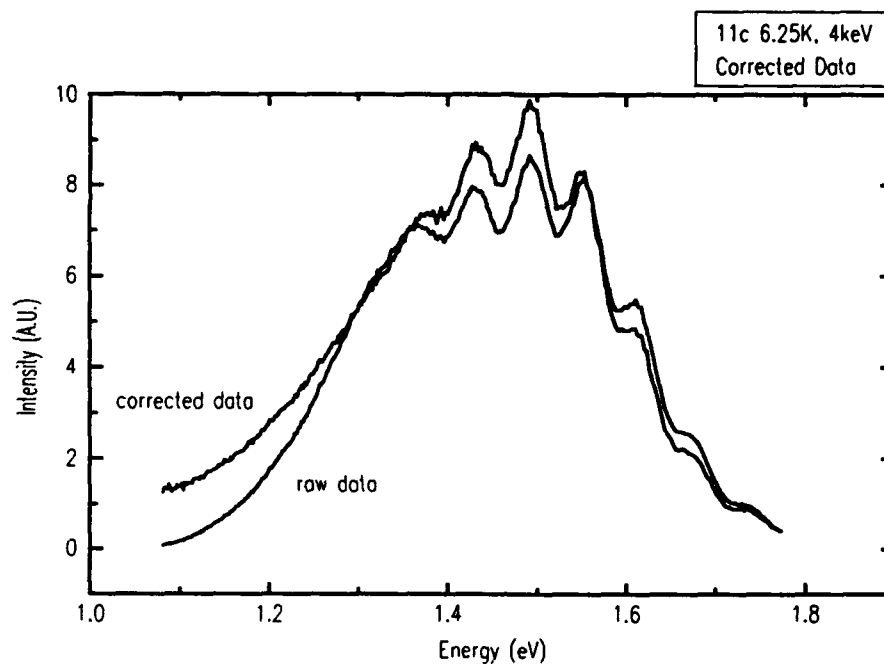
Figure 42. CL spectra of sample 11c showing data corrected for system response.
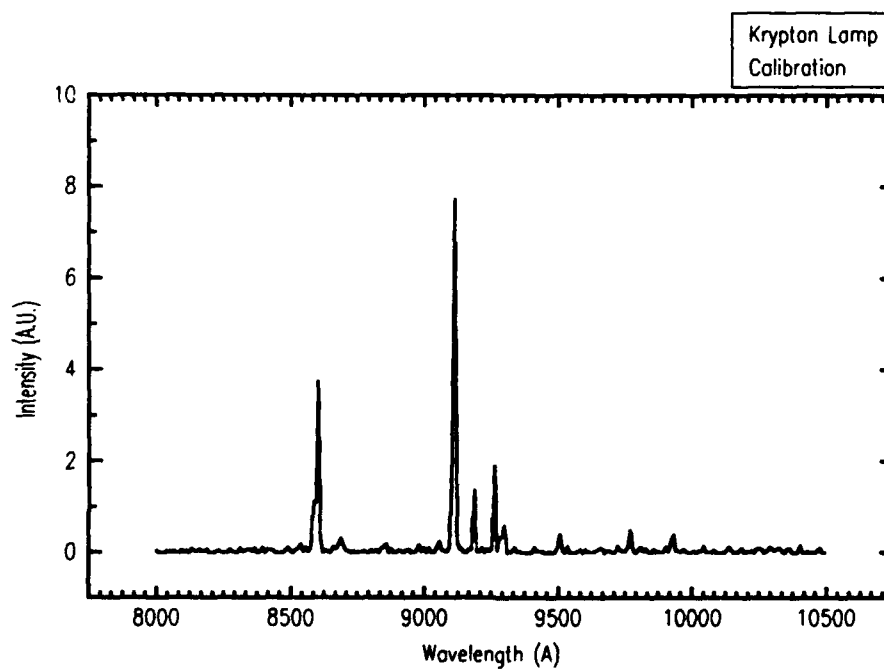
Figure 43. Spectrum showing Krypton lamp emission lines.

Appendix C

This appendix will elaborate on the penetration depth of the electrons into a $ZnGeP_2$ crystal.

From the periodic table the following information is gathered.

Table 1. Atomic Number and Weight of the Constituents

	Zn	Ge	P
Atomic Number	30	32	15
Atomic Weight (g/cm^3)	65.38	72.59	30.97
Atoms/ZnGeP$_2$ unit cell	4	4	8

The lattice constants are as follows: a =5.465 and c=10.771 angstroms. From this data the following approximations are made:

$$z_{ZnGe_2P} = \frac{z_{Zn} + z_{Ge} + 2\,z_P}{4} = 23 \tag{18}$$

$$\rho_{ZnGe_2P} = \frac{4\,A_{Zn} + 4\,A_{Ge} + 8\,A_P}{N_a \cdot c \cdot a} = 4.13 \ g/cm^3 \tag{19}$$

$$A = A_{Zn} + A_{Ge} + 2\,A_P = 199.92 \ g/mol. \tag{20}$$

As expressed in section 2.4.3, the mean rate of energy loss per segment of distance S traveled in the solid is expressed by the Bethe equation:

$$\frac{dE}{dS} = -2\,\pi q^4 N_A\,\frac{\rho Z}{EA}\,\ln\left[\frac{1.166\,E}{J}\right] \quad (14)$$

where q is the electronic charge, N_a is Avogadro's number, ρ is the density, A is the atomic weight, E is the mean electron energy, and J is the mean ionization potential. J is the average energy loss per interaction and is expressed in the following equation:

$$J = \left[9.76\,Z + 58.5\,Z^{-0.19}\right]10^{-3}\,(keV), \quad (15)$$

where Z is the atomic number. (31: 57)

Using the approximations for ρ, Z and A in ZnGeP$_2$, a 3 keV electron will lose 9.23×10^{-4} keV per angstrom traveled. The electron would travel 0.92 microns in a total "random walk" before its energy was dissipated. Obviously the electron will not travel in a straight line. The effective penetration range can be estimated by the Kanaya-Okayama variation of the Gruen range equation. (18:43)

$$R_e = \left[\frac{0.0276\,A}{\rho Z^{0.889}}\right] E^{1.67}\,(\mu m) \quad (16)$$

91

The penetration range for a 3 keV electron is 0.51 microns.

Data for different energy electrons are summarized in Table

2.

Table 2. Total Random walk and Penetration Depth for
Different Electron Energies.

Energy (keV)	dE/dS (keV/um)	Bethe (um)	Kanaya (um)
.5	8.16	.08	.03
1	1.77	.18	.08
2	4.87	.49	.26
3	9.23	.92	.51
4	1.48	1.5	.83

As can be observed from Table 2, as the electron energy
increases, the penetration depth to "random walk" distance
ratio increases. This says that highly energetic electrons
penetrate deeper and do not spread out in radial directions
as much as lower energy electrons.

Bibliography

1. Averkieva. G.K. et al. "Photoluminescence of p-Type $ZnGeP_2$ Crystals," Physica Status Solidi (a) **39**: 453-457 (1977).

2. Babonas, G. et al. "Wavelength-Modulated Absorption Spectra of Pseudo direct Bandgap $A^2C^4C^5_2$ Compounds," Physica Status Solidi (b) **62**: 327-334 (1974).

3. Bethe, H. Handbook of Physics, **24**. Berlin: Springer-Verlag, 1933.

4. Boyd, G.D. et al. "Linear and Nonlinear Optical Properties of $ZnGeP_2$ and CdSe," Applied Physics Letters, **18**: 301-304 (1971).

5. Boyd, Robert W. Radiometry and the Detection of Optical Radiation. New York: John Wiley & Sons, 1983.

6. Brudnyi, V.N. et al. Physica Status Solidi (a) **59**: 379 (1978).

7. Cohen, Marvin L. and James R. Chelikowsky. "Electronic Structure and Optical Properties of Semiconductors," Springer Series in Solid-State Sciences 75. Berlin: Springer-Verlag, 1989.

8. Dorian, John A. Photoluminescence Spectroscopy of MBE Grown Gallium Antimonide. MS thesis, AFIT/GEP/ENP/91D-4. School of Engineering, Air Force Institute of Technology (AU), Wright-Patterson AFB OH, December 1991.

9. France R.W. et al. "OH-Absorption in Fluoride Glass Infra-red Fibres," Electronics Letters, 20: 607 (1984).

10. Gentile, A.L. and O.M. Stafsudd. "Crystal Growth of $A^{II}B^{IV}C_2^V$ Chalcopyrites," Materials Research Bulletin, **9**: 105-116 (1973).

11. Ghandhi, Sorab K. VLSI Fabrication Principles Silicon and Gallium Arsenide. John Wiley & Sons: New York, 1983.

12. Goldstein, Herbert. Classical Mechanics. Reading, Massachusetts: Addison-Wesley Publishing Company, 1980.

13. Haynes, J.R. Physics Review Letters, 4: 361 (1960).

14. Hecht, Eugene. _Optics_. Reading, Massachusetts: Addison-Wesely Publishing Company, 1987.

15. Hedge, S.M. To Be Published.

16. Hobgood, H.M. et al. "Agile Laser Materials $ZnGeP_2$," Technical Report WL-TR-91-4083. WL/MLPO, Wright-Patterson AFB OH, 12 November 1991.

17. Hopfield, J.J. "The Quantum Chemistry of Bound Exciton Complexes," Proceedings of the 7th International Conference on the Physics of Semiconductors. Paris: Dunod, 1964.

18. Holt, D.B. and D.C. Joy. _SEM Microcharacterization of Semiconductors_. London: Academic Press, 1989.

19. Kanaya, K. and S. Okayama. "Penetration and Energy-Loss Theory of Electrons in Solid Targets," Journal of Physics D: Applied Physics, **5**: 43 (1972).

20. Leverenz, Humboldt W. _An Introduction to Luminescence of Solids_. New York: Dover Publications, 1968.

21. Levine, B.F. Physics Review, 7: 2591-2600 (1973).

22. McKelvey, John, P. _Solid State and Semiconductor Physics_. Malabar, Florida: Robert E. Krieger Publishing Company, 1966.

23. Menyuk, Norman and Paul Kelley. "Analysis of Nonlinear Optical Frequency Conversion," Technical Report ESD-TR-90-140. WL/AROF, Kirtland AFB NM, 8 January 1991.

24. Ohmer, M.C. "Breakthrough in Wavelength Tunable Infrared Laser Crystal Technology" to be published.

25. Ohmer, M.C. et al. "$ZnGeP_2$ Grown by the Liquid Encapsulated Czochralski Method." to be published.

26. Ohmer, M.C. Personal discussion. August 1992.

27. Pankove, Jacques L. _Optical Processes In Semiconductors_. New York: Dover Publications, 1971.

28. Schunemann, Peter G. "Agile Laser Materials: Crystal Growth of $ZnGeP_2$ for Optical Parametric Oscillator Applications," Technical Report WL-TR-91-4063. WL/MLPO, Wright-Patterson AFB OH, 1 November 1991.

29. Shaffer, Brad L. Analysis of Space Radiation Effects in Gallium Arsenide and Cadmium Selenide Semiconductor Samples Using Luminescence Spectroscopic Techniques. MS thesis, AFIT/GSO/ENP/90D-02. School of Engineering, Air Force Institute of Technology (AU), Wright-Patterson AFB OH, December 1990.

30. Shay, J.L. and J.H. Wernick. Ternary Chalcopyrite Semiconductors: Growth, Electronic Properties, and Applications. New York: Pergamon Press, 1975.

31. Sze, S.M. Semiconductor Devices Physics and Technology. New York: John Wiley & Sons, 1985.

32. Voevodin, V.G. et al. "Behavior of Impurity Copper in $ZnGeP_2$ Single Crystals With Diffusion Doping," Soviet Physics Journal **28**: 144-148 (1985).

33. Yacobi, B.G. and D.B. Holt. Cathodoluminescence Microscopy of Inorganic Solids. New York: Plenum Press, 1990.

34. Yariv, Amnon. Optical Electronics. Philadelphia: Saunders College Publishing, 1991.

Vita

Captain Michael R. Gregg was born on 25 March 1965 in Racine, Wisconsin. He graduated from T.C. Roberson High School in Skyland, North Carolina in 1983 and attended Wake Forest University, graduating with a Bachelor of Arts in Physics in May 1987. While attending Wake Forest, he obtained a Junior Fellowship at the National Climatic Data Center, NOAA, U.S. Chamber of Commerce. He obtained a reserve commission in the USAF after attending Officers Training School in June 1988. His first duty assignment was as a research physicist at Rome Laboratory, Hanscom AFB, MA. There he was responsible for developing an epitaxial growth system for III-V semiconductors. He entered the School of Engineering at the Air Force Institute of Technology in June 1991.

Permanent Address: 98 Bishop Cove Road
                        Fairview, North Carolina 28730

REPORT DOCUMENTATION PAGE

Public reporting burden for this collection of information is estimated to average 1 hour per response, including the time for reviewing instructions, searching existing data sources, gathering and maintaining the data needed, and completing and reviewing the collection of information. Send comments regarding this burden estimate or any other aspect of this collection of information, including suggestions for reducing this burden, to Washington Headquarters Services, Directorate for Information Operations and Reports, 1215 Jefferson Davis Highway, Suite 1204, Arlington, VA 22202-4302, and to the Office of Management and Budget, Paperwork Reduction Project (0704-0188), Washington, DC 20503.

1. AGENCY USE ONLY (Leave blank)	2. REPORT DATE	3. REPORT TYPE AND DATES COVERED
	3 Dec 92	Thesis

4. TITLE AND SUBTITLE

Cathodoluminescence Spectroscopy of Zinc Germanium Phosphide ZnGeP$_2$

5. FUNDING NUMBERS

6. AUTHOR(S)

Michael R. Gregg, Captain, USAF

7. PERFORMING ORGANIZATION NAME(S) AND ADDRESS(ES)

Air Force Institute of Technology
Engineering Physics Department
WPAFB, OH 45433

8. PERFORMING ORGANIZATION REPORT NUMBER

AFIT/GEP/ENP/92D-4

9. SPONSORING/MONITORING AGENCY NAME(S) AND ADDRESS(ES)

10. SPONSORING/MONITORING AGENCY REPORT NUMBER

N/A

11. SUPPLEMENTARY NOTES

12a. DISTRIBUTION/AVAILABILITY STATEMENT

Distribution unlimited; Approved for public release

12b. DISTRIBUTION CODE

13. ABSTRACT (Maximum 200 words)

Zinc Germanium Phosphide (ZnGeP$_2$) is a nonlinear semiconductor suitable for use as a laser tuning element over the two to six micron wavelength range. Although this crystal has been studied in the past, its luminescent properties are not yet well understood. In this present study, ZnGeP$_2$ has been examined using cathodoluminescence spectroscopy (CL). Specifically, the spectral dependence of the CL was obtained as a function of electron beam energy, beam current and temperature. The resulting CL was found to be polarized with a peak structure that was dependent on the polarization. This peak structure observed by CL is difficult to detect by photoluminescence (PL). It is believed that the peaks are due to transitions between the conduction band and the spin orbit split accepter level AL1. It is also believed that the excitation mechanism is in part responsible for the different structure observed.

14. SUBJECT TERMS

Zinc Germanium Phosphide, Cathodoluminescence
Photoluminescence, Non-linear Semiconductor

15. NUMBER OF PAGES
96

16. PRICE CODE

17. SECURITY CLASSIFICATION OF REPORT	18. SECURITY CLASSIFICATION OF THIS PAGE	19. SECURITY CLASSIFICATION OF ABSTRACT	20. LIMITATION OF ABSTRACT
UNCLASSIFIED	UNCLASSIFIED	UNCLASSIFIED	UNLIMITED

NSN 7540-01-280-5500

Standard Form 298 (Rev. 2-89)
Prescribed by ANSI Std Z39-18
298-102